ACS Partner Journal

Journal of the American Society for Mass Spectrometry

pubs.acs.org/jasms

Article

Nucleoside Cation Radicals: Generation, Radical-Induced Hydrogen Atom Migrations, and Ribose Ring Cleavage in the Gas Phase

Václav Zima, Owen Gladwish, Aleš Marek, and František Tureček*

Cite This: *J. Am. Soc. Mass Spectrom.* 2024, 35, 1594−1608

Read Online

ACCESS | Metrics & More | Article Recommendations | Supporting Information

ABSTRACT: Nucleoside ions that were furnished on ribose with a 2′-*O*-acetyl radical group were generated in the gas phase by multistep collision-induced dissociation of precursor ions tagged with radical initiator groups, and their chemistry was investigated in the gas phase. 2′-*O*-Acetyladenosine cation radicals were found to undergo hydrogen transfer to the acetoxyl radical from the ribose ring positions that were elucidated using specific deuterium labeling of 1′-H, 2′-H, and 4′-H and in the N−H and O−H exchangeable positions, favoring 4′-H transfer. Ion structures and transition-state energies were calculated by a combination of Born−Oppenheimer molecular dynamics and density functional theory and used to obtain unimolecular rate constants for competitive hydrogen transfer and loss of the acetoxyl radical. Migrations to the acetoxyl radical of ribose hydrogens 1′-H, 2′-H, 3′-H, and 4′-H were all exothermic, but product formation was kinetically controlled. Both Rice−Ramsperger−Kassel−Marcus (RRKM) and transition-state theory (TST) calculations indicated preferential migration of 4′-H in a qualitative agreement with the deuterium labeling results. The hydrogen migrations displayed substantial isotope effects that along with quantum tunneling affected the relative rate constants and reaction branching ratios. UV−vis action spectroscopy indicated that the cation radicals from 2′-*O*-acetyladenosine consisted of a mixture of isomers. Radical-driven dissociations were also observed for protonated guanosine, cytosine, and thymidine conjugates. However, for those nucleoside ions and cation radicals, the dissociations were dominated by the loss of the nucleobase or formation of protonated nucleobase ions.

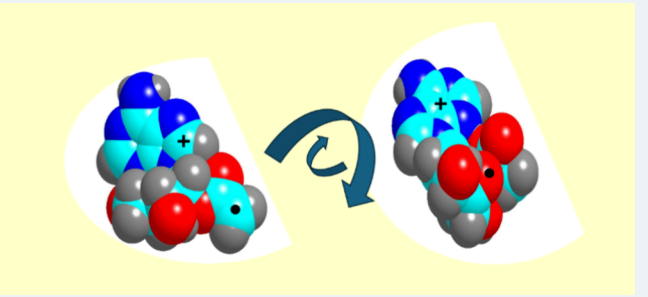

INTRODUCTION

Ionization of nucleic acids by radiation produces cation and anion radicals that undergo chemical reactions involving homolytic bond cleavages and proton or electron transfer reactions.[1−6] These reactions are fundamental for the complex process of nucleic acid damage which, when concerning DNA, has major implications in biology and medicine.[7] Because of the complexity of nucleic acids and the nonspecific nature of ionization that can initially affect any of the nucleobases, studies of nucleic acid ionization have focused on model oligonucleotides and chiefly used product analysis to identify stable downstream reaction products.[8−12] Proton and hydrogen atom migrations in reactive ion−radical intermediates of nucleic acids have been studied by UV−vis spectroscopy in aqueous solution[13−15] and by electron paramagnetic resonance (EPR) spectroscopy in frozen glasses.[16−18] Sevilla and coworkers have combined EPR with deuterium labeling to assign radical intermediates of photoinduced hydrogen abstraction from ribose positions in ionized adenosine[19] and guanosine.[20,21] These hydrogen transfers involved excited electronic states of the nucleobase cation radicals[21] and could occur as mono- or bimolecular reactions in the condensed phase.

An alternative approach to studying reactions of nucleic acid cation−radicals relies on the specific generation of reactive intermediates in the rarefied gas phase such as in the vacuum system of a mass spectrometer.[22] Under these conditions, cation radicals can be selected by mass and their unimolecular reactions can be monitored at a high level of sensitivity and specificity. Tandem mass spectrometry methods, such as UV−vis photodissociation action spectroscopy,[23] cyclic ion mobility,[24,25] and collision-induced dissociation (CID), have provided additional means for reactive radical intermediate characterization.[22] Bimolecular reactions of trapped ions, such as electron transfer[26,27] and hydrogen−deuterium exchange,[28] have also been utilized to characterize reactive nucleobase cation radicals.

We have applied charge-tagging methods to investigate reactions of nucleobase and sugar radicals in gas-phase ions. This consisted of docking the charge in a remote position to form a stable cation that is treatable by mass spectrometry and generating the radical at a specific site by CID or electron transfer.[29−31] In a previous study, we have used the radical-

Received: May 7, 2024
Revised: May 26, 2024
Accepted: May 29, 2024
Published: June 6, 2024

initiator method to investigate competitive hydrogen transfers to an acetyl radical, $^{\bullet}CH_2CO$, that was attached to ribose 5′-O in adenosine cation radicals (Figure 1).[32] The charge in those

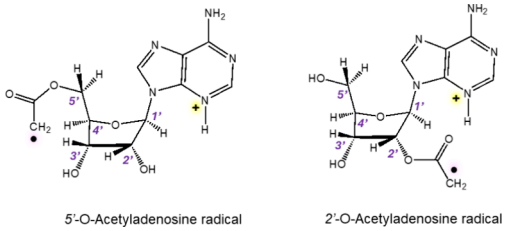

Figure 1. Protonated acetyladenosine radicals as reactive intermediates of ribose hydrogen atom transfer.

cation radicals was sequestered in the adenine ring at the most basic N-3 position, where it was stabilized by intramolecular hydrogen bonding to the ribose oxygens.[33] The stereochemistry of the 5′-O-based acetyl radicals was such that it allowed transfer of the *β*-facing ring hydrogen atoms from C-2′ and C-3′ as well as those from the adjacent C-5′ and sterically accessible C-4′ (Figure 1, left structure). This intramolecular hydrogen transfer has been shown to be kinetically controlled, favoring 3′-H and 5′-H, but exhibiting substantial primary isotope effects. The hydrogen atom at C-1′, which if transferred would have given rise to a C-1′ radical that according to calculations was the global energy minimum, was sterically inaccessible and thus nonreactive.[32]

In the present study, we explore the regioselectivity and stereoselectivity of ribose hydrogen migrations in nucleoside cation radicals in which the acetyl radical was placed at 2′-O. In this way, radical-initiated transfer of *α*-facing ring hydrogen atoms, 1′-H and 4′-H, should be enabled as well as that of the adjacent 2′-H (Figure 1, right structure). Similar to our previous study,[32] the acetyl radicals were generated by CID of mass-selected ions that carried a radical initiator in the form of 4,4′-azobis(4-cyanopentanoic acid) or its *N*-ethylamide (Scheme 1). This method has been used previously with charged peptide[34] and carbohydrate conjugates[35] where it allowed for site-specific radical generation to trigger further unimolecular reactions. Here, we use it to initiate and study radical-induced ribose-ring cleavages in nucleoside ions. In order to distinguish isomeric products of hydrogen atom transfer and ring cleavage reactions, we employed conjugates that were specifically labeled with deuterium at C-1′, C-2′, and C-4′ and in the exchangeable OH and NH positions, forming the respective adenosine radicals $\mathbf{A}_{1'\text{-D}}{}^{+\bullet}$, $\mathbf{A}_{2'\text{-D}}{}^{+\bullet}$, $\mathbf{A}_{4'\text{-D}}{}^{+\bullet}$, and $\mathbf{A}_{\text{D5}}{}^{+\bullet}$ (Scheme 1). To provide detailed structure and energy analysis of all relevant species, including intermediates and transition states, we carried out an extensive conformational search using Born−Oppenheimer molecular dynamics (BOMD) calculations and full gradient optimization by density functional theory (DFT). Reaction kinetics, including isotope effects and quantum tunneling, was addressed by Rice−Ramsperger−Kassel−Marcus (RRKM) and transition-state theory (TST) calculations. We wish to show that hydrogen atom migrations and subsequent ribose ring cleavages are controlled kinetically, not thermodynamically.

EXPERIMENTAL SECTION

Materials. Adenosine, guanosine, cytidine, and thymidine were purchased from Sigma-Aldrich (St. Louis, MO). Conjugates of adenosine, guanosine, and cytidine that were esterified at 2′-O with 4,4′-azobis(4-cyanopentanoic acid-*N*-ethylamide), $\mathbf{A_P}$, $\mathbf{G_P}$, and $\mathbf{C_P}$, were synthesized as shown for $\mathbf{A_P}$ in Scheme 2. The thymidine conjugate, $\mathbf{T_P}$, was esterified with 4,4′-azobis(4-cyanopentanoic acid). The synthesis involved selective protection at 5′-O and 3′-O as a cyclic tetraisopropyldisiloxane ether and protection of the adenine amine group as an *N*,*N*-dimethylamidine. Esterification at 2′-O with 4,4′-azobis(4-cyanopentanoic acid-*N*-ethylamide) followed by deprotection yielded conjugate $\mathbf{A_P}$. An analogous reaction sequence was employed to synthesize all deuterium-labeled adenosine conjugates as well as the cytidine conjugate $\mathbf{C_P}$. Synthesis of the guanosine and thymidine conjugates, $\mathbf{G_P}$ and $\mathbf{T_P}$, respectively, required only protection at 5′-O and 3′-O. Synthetic details and product characterization by NMR and

Scheme 1. Generation of 2′-*O*-Acetyladenosine Radicals $A^{+\bullet}$, and Structures of Deuterium-Labeled Analogues $\mathbf{A}_{1'\text{-D}}{}^{+\bullet}$, $\mathbf{A}_{2'\text{-D}}{}^{+\bullet}$, $\mathbf{A}_{4'\text{-D}}{}^{+\bullet}$, and $\mathbf{A}_{\text{D5}}{}^{+\bullet}$

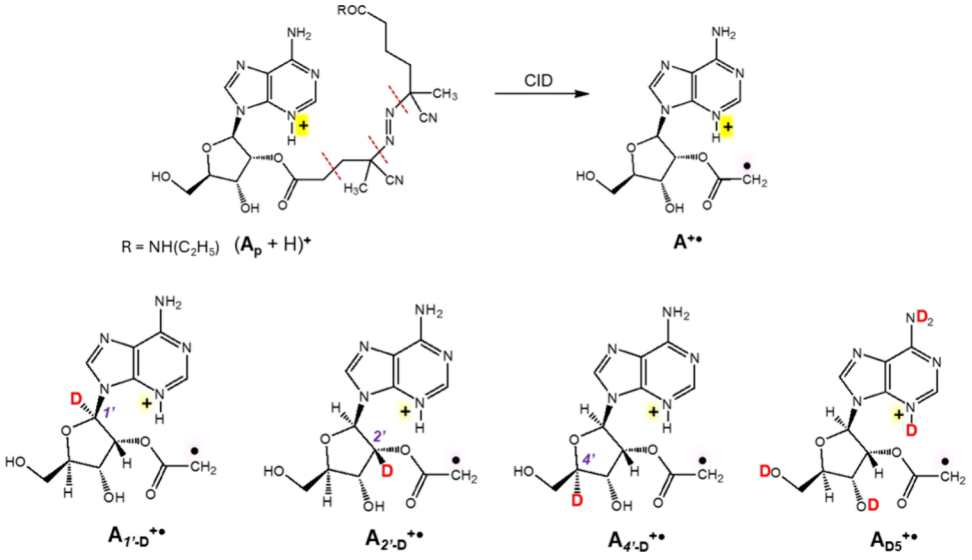

https://doi.org/10.1021/jasms.4c00198
J. Am. Soc. Mass Spectrom. 2024, 35, 1594−1608

Scheme 2. Synthesis of Nucleoside Conjugates[a]

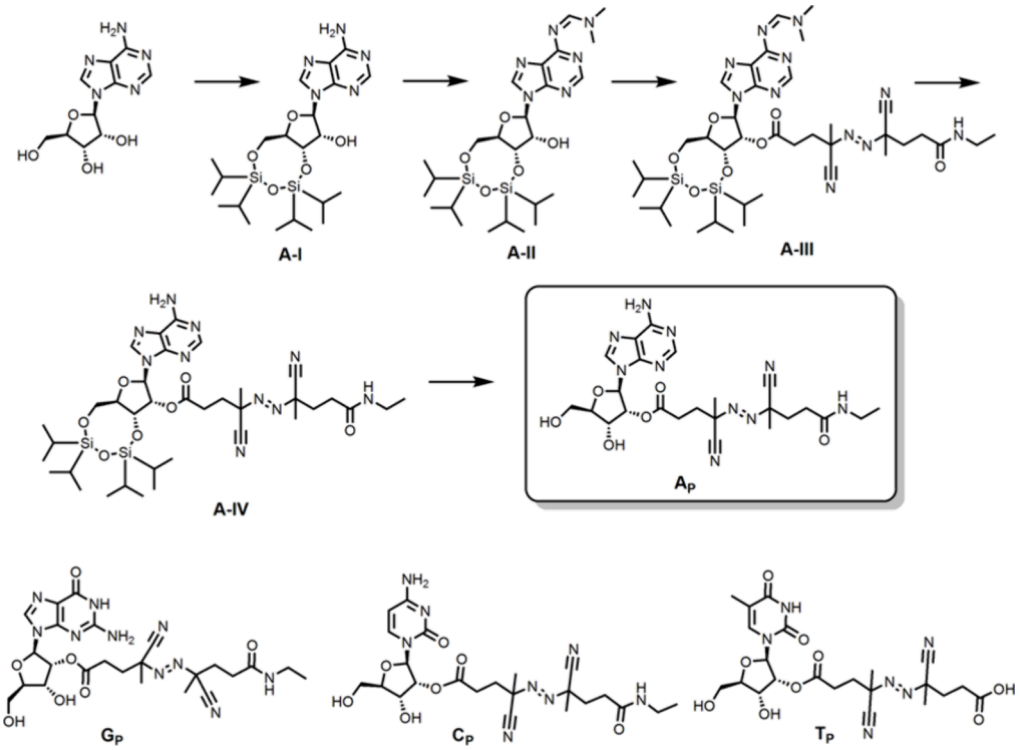

[a]Reagents, solvents, and experimental details are given in the Supporting Information.

high-resolution mass spectrometry are given in the Supporting Information.

Methods. Mass spectra were measured on a Bruker amaZon 3D ion trap tandem mass spectrometer that was modified for photodissociation action spectroscopy, as described previously.[36] Ions were produced by electrospray ionization from 50:50 water−methanol solutions containing 1% of acetic acid. Ions were selected by mass and excited by collisions with helium to produce CID-MS spectra. Action spectra were measured in three wavelength regions that were scanned in 2 nm steps for 210−354 and 355−409 nm and in 5 nm steps over 410−700 nm. The light beam was produced from an NL301G (Altos Photonics, Bozeman, MT, USA) Nd:YAG laser (20 Hz) and directed into a PG142 unit consisting of an optical parametric oscillator that was coupled to a second-harmonic generator. The laser pulse energies typically ranged between 0.2 and 4.0 mJ per pulse, as measured at each wavelength and used to calibrate the action spectra. The reported action spectrum is an average of two measurements taken on different days. High-resolution mass spectra were measured on an Orbitrap Ascend Tribrid instrument (ThermoFisher, San Jose, CA) at a 100 000 resolving power. All ion assignments were corroborated by elemental compositions that were based on accurate m/z.

Calculations. Structures were generated by Born−Oppenheimer molecular dynamics (BOMD) calculations that were run for 20 ps with 1 fs steps using the Berendsen thermostat[37] at 510 and 610 K. Initial adenine protonation was at N-3, which is known to be the most basic position in adenosine.[33] These trajectory calculations were performed with PM6-D3H4[38] which complements the semiempirical Hamiltonian with dispersion and hydrogen-bonding interactions. The high-end Cuby4 platform[39] was used in all trajectory calculations using MOPAC.[40] Two hundred snapshots were selected at regular intervals from 20 000 points in the BOMD trajectories and fully gradient optimized with PM6-D3H4. Several selected low-energy structures were further optimized with B3LYP[41] to provide harmonic frequencies and then reoptimized with M06-2X.[42] These calculations were run with the 6-31+G(d,p) basis set within the spin-unrestricted open-shell formalism. The M06-2X/6-31+G(d,p)-optimized geometries were used to calculate single-point energies which were carried out with M06-2X and the aug-cc-pVTZ,[43] def2tzvpp,[44] and def2qzvpp[45] basis sets. Calculations with the aug-cc-pVTZ (1357 basis functions) and def2qzvpp (1704 basis functions) basis sets gave very similar relative energies with a 0.9 kJ mol^{-1} root-mean-square deviation. Excited states were calculated by time-dependent density functional theory (TD-DFT)[46] using M06-2X/6-31+G(d,p). Previous benchmarking to equation-of-motion CCSD calculations has shown that M06-2X was adequate for excitation energies and oscillator strength calculations of peptide and nucleic acid cation radicals.[47,48] Atomic charge and spin densities were calculated by natural population analysis (NPA)[49] of the M06-2X/def2qzvpp wave functions. All standard DFT calculations were run with Gaussian 16 (Revision B.01) that was licensed from Gaussian, Inc. (Wallingford, CT). Vibronic absorption spectra were obtained from TD-DFT calculations of vertical excitation in 300 Wigner configurations[50,51] at 350 K that were produced from normal coordinates and sorted out according to their Boltzmann factors. Typically, 25−30 excited states were used in vibronic spectra calculations. These calculations were run under Newton X, Version 2.0.[52] Rice−Ramsperger−Kassel−Marcus (RRKM)[53] calculations of unimolecular rate constants were run with the QCPE program[54] that was recompiled[55] and run under Windows 10. Transition-state energies were taken

https://doi.org/10.1021/jasms.4c00198
J. Am. Soc. Mass Spectrom. 2024, 35, 1594−1608

from the M06-2X/aug-cc-pVTZ calculations; scaled harmonic frequencies and moments of inertia were from the 6-31+G(d,p)-optimized structures. Rotations were treated adiabatically, and the microscopic $k(E, J, K)$ rate constants were Boltzmann averaged over the distribution of rotational states at 310 K. Tunneling effects[56] were approximated by analysis of parabolic barriers using the potential energy surface curvature in the transition states as inferred from the imaginary frequencies for the motion along the reaction coordinates. Harmonic frequencies were scaled by 0.975. Intrinsic reaction coordinate (IRC) calculations[57] were performed on M06-2X/6-31+G(d,p) potential energy surfaces to connect transition states to reactants and products.

RESULTS AND DISCUSSION

Adenosine Radicals. Acetyladenosine cation radicals were generated by two-step CID of the $(\mathbf{A}_p + H)^+$ precursor ions at m/z 557 as shown in Scheme 1. The relevant spectra are shown in Figure S1a (Supporting Information). In the first step, CID-MS^2 resulted in the combined loss of N_2 and the $C_8H_{13}N_2O$ ethylamide side chain, forming a fragment ion at m/z 376 (Figure S1a). This ion was isolated and subjected to the next CID-MS^3 step, leading to loss of methylpropene nitrile (C_4H_5N) and formation of the acetyladenosine cation radical $\mathbf{A}^{+\bullet}$ (m/z 309.1050, $C_{12}H_{15}N_5O_5$, Figure S1b). This sequence was analogous to that used for the generation of adenosine-5′-*O*-acetyl radicals.[32] The deuterium-labeled ions, $\mathbf{A}_{1'\text{-D}}{}^{+\bullet}$, $\mathbf{A}_{2'\text{-D}}{}^{+\bullet}$, $\mathbf{A}_{4'\text{-D}}{}^{+\bullet}$, and $\mathbf{A}_{D5}{}^{+\bullet}$, were generated analogously from the respective labeled conjugates.

CID-MS^4 of $\mathbf{A}^{+\bullet}$ (Figure 2) furnished a spectrum that displayed major dissociations forming fragment ions by loss of $CH_3CO^\bullet$ (m/z 266) and $CH_3COO^\bullet$ (m/z 250). Formation of these fragment ions involved hydrogen transfer to the acetyl radical followed by cleavage of the CH_3CO-O and $CH_3COO-C\text{-}2'$ bonds, respectively. In addition, ring cleavage resulted in the formation of a $C_6H_6N_5O^+$ (m/z 164) fragment ion which was identified as protonated 9-formyladenine on the basis of deuterium labeling at C1′ (Figure S2b, Supporting Information). A glycosidic bond cleavage gave protonated adenine ($C_5H_6N_5^+$) at m/z 136. Several minor fragment ions were formed either directly from $\mathbf{A}^{+\bullet}$ or by consecutive dissociations of the ribose ring. Loss of acetic acid proceeded from $\mathbf{A}^{+\bullet}$, giving rise to a weak fragment ion at m/z 249 (<5%). Consecutive dissociations of the prominent m/z 250 ions formed ions at m/z 202 by loss of ($CH_2O + H_2O$) and m/z 201 by loss of ($C_3H_6O_3 + H_2O$), as established by accurate mass measurements. It should be noted that the fragment ion relative intensities somewhat depended on the experimental conditions, in particular, collisional activation in the 3D ion trap or quadrupole mass analyzer. Full spectra comparisons are given in Figures S2a–c (Supporting Information).

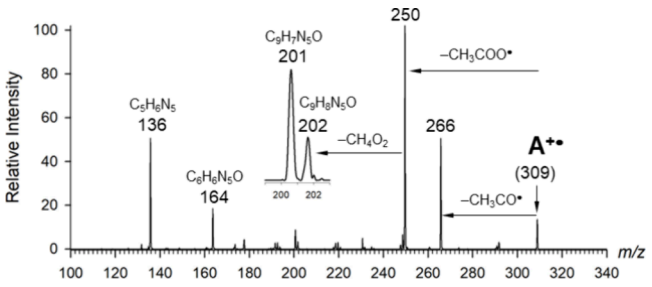

Figure 2. CID-MS^4 spectrum of 2′-*O*-acetyladenosine cation radical $\mathbf{A}^{+\bullet}$ (m/z 309.1050, $C_{12}H_{15}N_5O_5$).

Deuterium labeling allowed us to identify the fragment ions and track the hydrogen atoms that were involved in the migrations. Starting with protonated adenine whose formation requires a hydrogen atom transfer onto the nucleobase, we found that 1′-H was involved at only ca. 1%, as evidenced by the ratio of the m/z 137 and 136 ion intensities in the spectrum of $\mathbf{A}_{1'\text{-D}}{}^{+\bullet}$ (Figure 3). A substantial fraction of hydrogen atom transfer involved 2′-H, as shown by a 64% fraction of m/z 137 ($C_5H_5DN_5^+$) in the spectrum of $\mathbf{A}_{2'\text{-D}}{}^{+\bullet}$ (Figure 3). The contribution of 4′-H was minor in $\mathbf{A}_{4'\text{-D}}{}^{+\bullet}$ (5%), indicating that this hydrogen was not substantially transferred to adenine. The OD groups in $\mathbf{A}_{D5}{}^{+\bullet}$ collectively contributed 30% of deuterium transfer to adenine (Figure 3).

Loss of acetoxyl radical was the most prominent dissociation of the 2′-*O*-acetyladenosine cation radicals (Figure 2). The dissociation required a hydrogen atom to be transferred onto the $^\bullet CH_2COO$ group from a sterically accessible position on the ribose or adenine moieties. The results obtained by deuterium labeling (Figure 4) showed low participation by 1′-D, 2′-D, and all exchangeable D in the acetoxyl loss. Accurate mass measurements established that the weak peaks at m/z 250 from $\mathbf{A}_{1'\text{-D}}{}^{+\bullet}$ and $\mathbf{A}_{2'\text{-D}}{}^{+\bullet}$ in Figure 4 were entirely due to the loss of acetic acid (Δm = 60.0211 Da, $C_2H_4O_2$). The main source of deuterium came from 4′-D, amounting to up to 55% of the acetoxyl loss. The high-resolution CID-MS^4 spectrum of

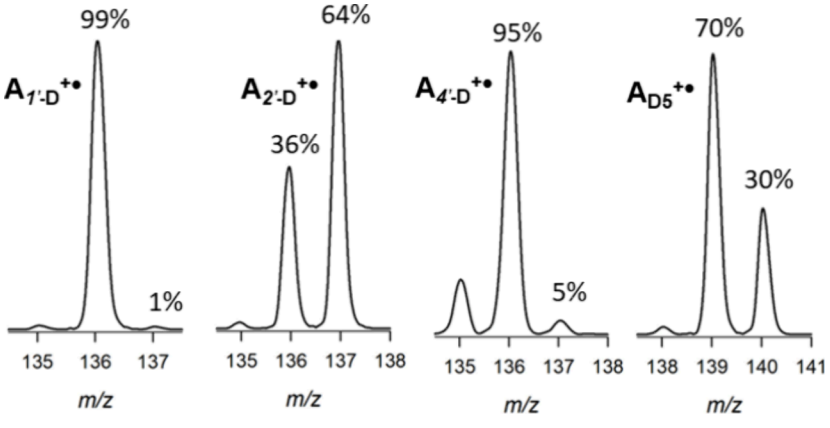

Figure 3. Intensity profiles of isotopologues of the $C_5H_6N_5^+$ fragment ion. The percentages are based on integrated peak areas.

https://doi.org/10.1021/jasms.4c00198
J. Am. Soc. Mass Spectrom. 2024, 35, 1594−1608

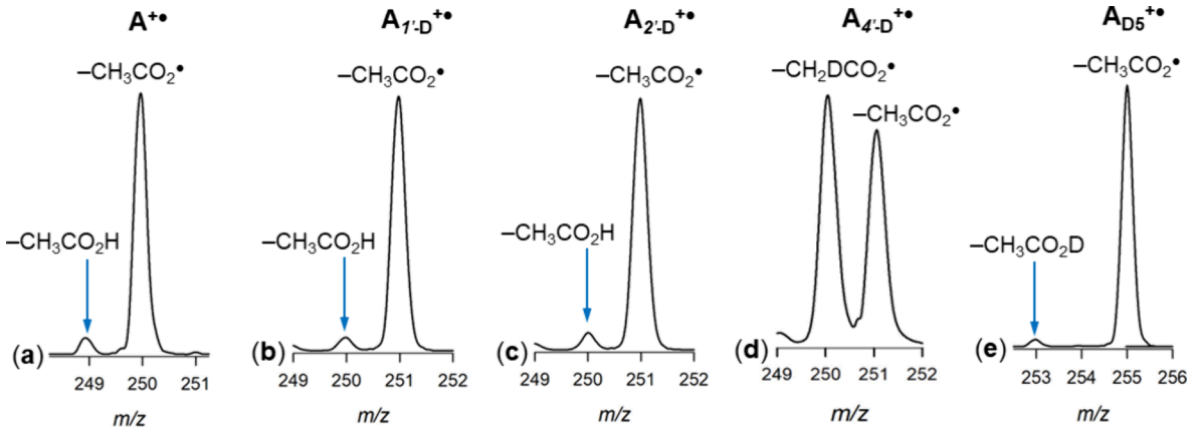

Figure 4. Intensity profiles of isotopologues of the fragment ion by loss of $CH_3COO^•$ from (a) $A^{+•}$, (b) $A_{1'\text{-}D}{}^{+•}$, (c) $A_{2'\text{-}D}{}^{+•}$, (d) $A_{4'\text{-}D}{}^{+•}$, and (e) $A_{D5}{}^{+•}$.

the m/z 310.1128 $(C_{12}H_{14}DN_5O_5)^{+•}$ ion from $A_{4'\text{-}D}{}^{+•}$ showed a 100/85 ratio of the [m/z 250.0933]/[m/z 251.0996] ion intensities corresponding to the respective losses of $CH_2DCOO^•$ and $CH_3COO^•$. The high-resolution data indicated that the contribution of CH_3COOH loss from $A_{4'\text{-}D}{}^{+•}$ at m/z 250.0918 was negligible.

Loss of acetyl radical (Δm = 43.0183 from high-resolution measurements) was a major dissociation of the 2′-*O*-acetyladenosine cation radicals that was characteristic for the acetyl radical at 2′-O (Figure 2), which distinguished it from the 5′-*O*-acetyl radicals reported previously.[32] The spectra of the deuterium-labeled radicals revealed practically no involvement in the acetyl loss of deuterium atoms from the labeled positions. This was indicated by the CID-MS^4 spectra that showed no mass shift for the fragment ions, giving m/z 267 for loss of $CH_3CO^•$ from $A_{1'\text{-}D}{}^{+•}$, $A_{2'\text{-}D}{}^{+•}$, and $A_{4'\text{-}D}{}^{+•}$ and m/z 271 by loss of $CH_3CO^•$ from $A_{D5}{}^{+•}$ (Figure 5). Evidently, the

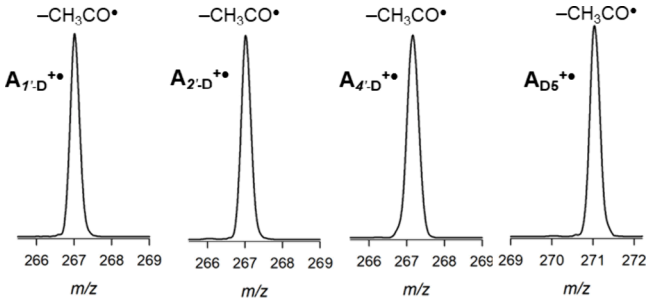

Figure 5. Intensity profiles of isotopologues of the fragment ion by loss of $CH_3CO^•$.

formation of the acetyl group must have been triggered by a hydrogen transfer from an unlabeled ribose (H-3′ or H-5′) or adenine (H-2 or H-8) position that must have differed from the isomerization that preceded the loss of $CH_3COO^•$ (Figure 4).

The nature of the primary m/z 267 and 250 fragment ions was further investigated by CID-MS^5 in combination with deuterium labeling. Upon collisional activation, both of these even-electron ions dissociated by loss of the ribose residue to form prominent $C_5H_6N_5{}^+$ ions of protonated adenine. However, the distribution of deuterium in the protonated adenine in the CID-MS^5 spectra of these even-electron ions was different from those originating from the radicals. For example, the spectrum of the m/z 267 ion (loss of $CH_3CO^•$) from $A_{2'\text{-}D}{}^{+•}$ (Figure S3a) showed a different [$C_5H_6N_5{}^+$]/[$C_5H_5DN_5{}^+$] fragment ion ratio, favoring the light ion, which indicated that the proton transferred onto the adenine moiety also originated from ring positions other than C-2′. The spectrum of the m/z 267 ion from $A_{1'\text{-}D}{}^{+•}$ further indicated that deuterium transfer from C-1′ was absent (Figure S3b). In contrast, the spectra of the m/z 251 ions by loss of $CH_3COO^•$ from $A_{2'\text{-}D}{}^{+•}$ and $A_{1'\text{-}D}{}^{+•}$ were indistinguishable (Figure S3c and S3d), both showing a dominant formation of protonated adenine (m/z 136) by glycosidic bond cleavage.

Adenosine Cation−Radical Structures and Energies. Ion dissociations in combination with deuterium labeling indicated the main radical-driven reactions of the gas-phase ions. To further characterize the relevant species and their reactivity, we obtained the optimized structures and relative energies of the starting 2′-*O*-acetyladenosine cation radical, its several isomers, transition states for isomerization, reaction intermediates, and products. The calculated energies relative to the lowest energy conformer of 2′-*O*-acetyladenosine cation radical ($\mathbf{1}^{+•}$) are compiled in Table 1; the M06-2X/def2qzvpp energies along with zero-point vibrational energies were used to display 0 K enthalpies and 310 K Gibbs energies (italic numerals) in reaction schemes that in each case refer to the particular reactant (Schemes 3−8).

1′-H-Migration onto the acetyl radical in $\mathbf{1}^{+•}$ was mildly exothermic, $\Delta G_{310}(\mathbf{1}^{+•} \rightarrow \mathbf{2}^{+•})$ = −25 kJ mol^{-1}, forming the 1′-radical $\mathbf{2}^{+•}$. Structure $\mathbf{2}^{+•}$ showed partial separation of atomic charge and spin density between the adenine ring and the ribose moiety, as determined from natural population analysis (NPA)[49] of the UM06-2X/def2qzvpp wave function. Adenine ring protonation contributed 67% of ion charge, whereas 90% of the spin density was in the ribose ring where 1′-C (76%) and the ring oxygen atom (10%) were the major spin sites. This distribution was similar to that reported for protonated 2′-deoxyadenosin-1′-yl radical that carried a combined 89% of spin density within the 2′-deoxyribose ring.[58] The separation of charge and spin density in different parts of the cation radical satisfied the classification of $\mathbf{2}^{+•}$ as a distonic ion.[59,60] The isomerization by 1′-H migration proceeded via a six-membered cyclic transition state (**TS1**) that was 139 kJ mol^{-1} above $\mathbf{1}^{+•}$ (Scheme 3). **TS1** had the characteristics of an early transition state, as evidenced by the different distances between the migrating 1′-H and the 1′-C and acetyl carbons. The overall conformation of the adenosine moiety was conserved

https://doi.org/10.1021/jasms.4c00198
J. Am. Soc. Mass Spectrom. 2024, 35, 1594−1608

Table 1. Relative Energies of 2′-Acetyladenosine Cation Radicals

	relative energy[a,b]		
ion/reaction	M06-2X/6-31+G (d,p)	M06-2X/aug-cc-pVTZ	M06-2X/def2qzvpp
$\mathbf{1}^{+\bullet}$	0.0	0.0	0.0
$\mathbf{2}^{+\bullet}$	−18	−20	−21
$\mathbf{3}^{+\bullet}$	−6.4	−9.2	−10
$\mathbf{4}^{+\bullet}$	−38	−41	−41
$\mathbf{5}^{+\bullet}$	−23	−26	−26
$\mathbf{6}^{+\bullet}$	1.0	3.4	3.9
TS1	140	140	139
TS2	145	146	146
TS3	150	148	148
TS4	125	124	124
TS5	102	94	94
$\mathbf{7}^{+\bullet}$	16	4.3	3.3
TS6	106	94	94
$\mathbf{8}^{+\bullet}$	103	88	87
$\mathbf{9}^{+}$ + $CH_3COO^{\bullet}$	140	128	125
TS7	156	145	144
$\mathbf{10}^{+\bullet}$	85	72	70
$\mathbf{11}^{+}$ + $CH_3CO^{\bullet}$	118	112	108

[a]In kJ mol^{-1}. [b]Including B3LYP/6-31+G(d,p) zero-point energies and referring to 0 K.

Scheme 3. Optimized Structures and Energies for $\mathbf{1}^{+\bullet} \rightarrow \mathbf{2}^{+\bullet}$ Isomerization

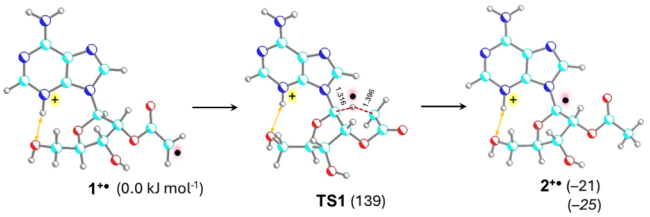

upon reaching **TS1** from $\mathbf{1}^{+\bullet}$, as judged by the N3−H···5′-O hydrogen bond that remained at 1.910−1.912 Å. The geometry flattening at 1′-C upon hydrogen abstraction forced an elongation of the N3−H···5′-O hydrogen bond to 1.959 Å in $\mathbf{2}^{+\bullet}$.

Isomerization by 2′-H migration in $\mathbf{1}^{+\bullet}$ was calculated to be mildly exothermic, $\Delta G_{310}(\mathbf{1}^{+\bullet} \rightarrow \mathbf{3}^{+\bullet}) = -14$ kJ mol^{-1}, forming the 2′-radical $\mathbf{3}^{+\bullet}$ (Scheme 4). NPA of $\mathbf{3}^{+\bullet}$ showed 98% of spin

Scheme 4. Optimized Structures and Energies for $\mathbf{1}^{+\bullet} \rightarrow \mathbf{3}^{+\bullet}$ Isomerization

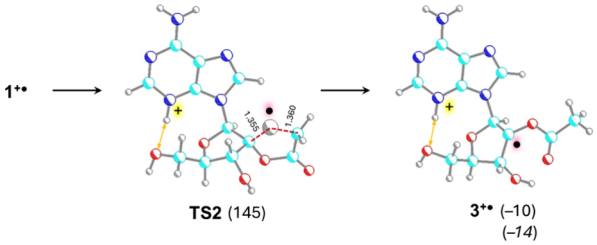

density within the ribose ring with 2′-C (83%), 2′-O (6%), and 3′-O (5%) being the major spin-density carrying sites. The positive charge was partitioned between the protonated adenine and acetylribose moieties in a 65/35 ratio. The pertinent transition state for 2′-H migration (**TS2**) was at 146 kJ mol^{-1} relative to $\mathbf{1}^{+\bullet}$ and involved a five-membered cyclic arrangement of the involved atoms. **TS2** showed very similar distances of the migrating 2′-H from 2′-C and the receiving acetyl methylene carbon (Scheme 4).

In contrast to 1′-H and 2′-H that were sterically accessible to the acetyl radical in $\mathbf{1}^{+\bullet}$, 3′-H was situated on the opposite (β) face of the ribose ring, which necessitated a dihedral angle distortion for 3′-H migration to occur in order to form the new C−H bond. This was reflected by the geometry of the pertinent transition state for 3′-H migration (**TS3**) as shown in Scheme 5. The migration, forming radical $\mathbf{4}^{+\bullet}$, was calculated

Scheme 5. Optimized Structures and Energies for $\mathbf{1}^{+\bullet} \rightarrow \mathbf{4}^{+\bullet}$ Isomerization

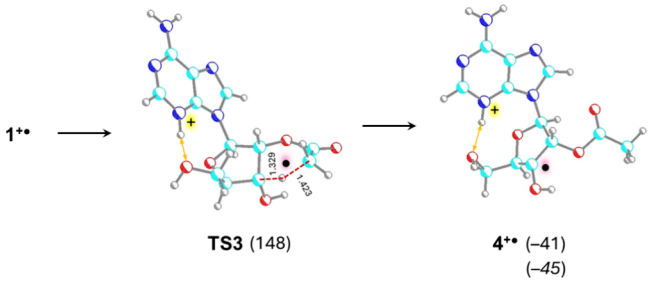

to proceed via a six-membered cycle in which 3′-H was brought to the acetyl carbon within 1.423 Å, indicating an early transition state. Reaching **TS3** was associated with a substantial distortion of the 3′-H−3′-C−2′-C−2′-O dihedral angle that went from 154° in $\mathbf{1}^{+\bullet}$ to 6° in **TS3.**

This distortion imposed strain on the ribose ring that resulted in a significantly higher energy for **TS3**, which was at 148 kJ mol^{-1} relative to $\mathbf{1}^{+\bullet}$. The TS energy increase may be slightly mitigated by the shorter hydrogen bond between N3−H and 5′-O in **TS3** (1.858 Å) compared to that in $\mathbf{1}^{+\bullet}$ (1.912 Å). Overall, the $\mathbf{1}^{+\bullet} \rightarrow \mathbf{4}^{+\bullet}$ isomerization was substantially exothermic with $\Delta G_{310}(\mathbf{1}^{+\bullet} \rightarrow \mathbf{4}^{+\bullet}) = -45$ kJ mol^{-1}, forming the 3′-radical as the global energy minimum of the 2′-*O*-acetyladenosine cation radical set. The spin density in $\mathbf{4}^{+\bullet}$ was

https://doi.org/10.1021/jasms.4c00198
J. Am. Soc. Mass Spectrom. 2024, 35, 1594−1608

almost exclusively (>99%) localized within the ribose ring with 3′-C (79%) and 3′-O (13%) being the major contributors.

Migration of 4′-H was calculated to have the lowest TS energy (124 kJ mol^{-1} relative to $\mathbf{1}^{+\bullet}$) and proceeded via an eight-membered cyclic transition state (**TS4**, Scheme 6). The

Scheme 6. Optimized Structures and Energies for $\mathbf{1}^{+\bullet} \rightarrow \mathbf{5}^{+\bullet}$ Isomerization

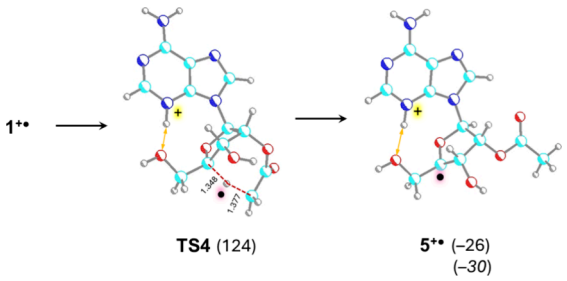

isomerization formed cation radical $\mathbf{5}^{+\bullet}$ that was at ΔG_{310} = −30 kJ mol^{-1} relative to $\mathbf{1}^{+\bullet}$. Ion $\mathbf{5}^{+\bullet}$ was another example of a distonic ion in which the charge and spin densities were separated between the adenine and the ribose rings. Most of the spin density was carried by 4′-C (84%) and ring-O (10%) with minor delocalization onto nearby 5′-O (3%) and 3′-H (3%). Regarding the hydrogen migration to $^{\bullet}CH_2COO$, reaching 4′-H required conformational changes in the ribose ring as evidenced by the 4′-H−4′-C−3′-C−3′-O dihedral angle that changed from −31° in $\mathbf{1}^{+\bullet}$ to −51° in **TS4.** As a result, **TS4** developed a shorter N3−H···5′-O hydrogen bond (1.722 Å), which may have contributed to its stabilization and lower energy (Scheme 6).

The distonic nature of $\mathbf{2}^{+\bullet}$−$\mathbf{5}^{+\bullet}$ sharply contrasted with the electronic structure of the canonical 2′-*O*-acetyladenosine cation radical ($\mathbf{6}^{+\bullet}$). Ion $\mathbf{6}^{+\bullet}$ showed ca. 90% of spin density to be delocalized among several atoms in the adenine ring (Figure 6). In addition, the canonical isomer was less thermodynamically stable than the distonic ions, as discussed previously for 2′-deoxyadenosine.[58]

Further reactions of the intermediate C-based radicals were computationally studied for $\mathbf{5}^{+\bullet}$, which was indicated to be involved in hydrogen transfer on the basis of experimental deuterium labeling results. The radical site at 4′-C was

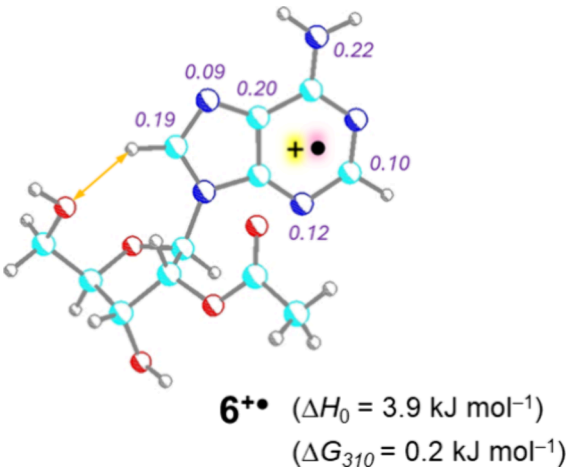

Figure 6. Canonical isomer $\mathbf{6}^{+\bullet}$ with NPA atomic spin densities. The energies are relative to $\mathbf{1}^{+\bullet}$.

expected to promote homolytic cleavage of the bonds at the adjacent atoms, O−1′-C and 3′-C−2′-C, respectively, via a standard β-elimination mechanism. The reaction sequence initiated by cleavage of the O−1′-C bond is shown in Scheme 7. The transition state (**TS5**) was found at an O−1′-C bond elongation to 1.844 Å, indicating an early transition state at 120 kJ mol^{-1} above $\mathbf{5}^{+\bullet}$. The continuing bond cleavage was associated with a conformational change that strengthened the 4′-O···3-H hydrogen bond in intermediate $\mathbf{7}^{+\bullet}$. The ring opening in $\mathbf{5}^{+\bullet}$ was overall 29 kJ mol^{-1} endothermic. The radical at 1′-C in $\mathbf{7}^{+\bullet}$ weakened the 2′-C−2′-O bond that dissociated reaching a transition state (**TS6**) at 120 kJ mol^{-1} above $\mathbf{5}^{+\bullet}$ (Scheme 7). The low **TS6** energy was achieved owing to a conformational change that formed a strong hydrogen bond between the leaving acetoxy group and the charging proton at N-3 (Scheme 7). Past **TS6**, the loss of the acetoxyl radical proceeded via an ion−radical complex ($\mathbf{8}^{+\bullet}$, 113 kJ mol^{-1} above $\mathbf{5}^{+\bullet}$) to reach the thermochemical threshold of the product ion $\mathbf{9}^{+}$ at 151 kJ mol^{-1}. The TS energies at **TS5** and **TS6** (Scheme 7) can be compared with that of **TS4** (Scheme 6) when expressed as a reverse hydrogen migration in $\mathbf{5}^{+\bullet}$ ($E_{TS,rev}$ = 150 kJ mol^{-1}, relative to $\mathbf{5}^{+\bullet}$). These TS energies indicated that **TS4** for the 4′-H migration in $\mathbf{1}^{+\bullet}$ was the highest saddle point on the potential energy surface, leading to acetoxyl radical loss and forming ion $\mathbf{9}^{+}$. The comparable energies for **TS4** and the ($\mathbf{9}^{+}$ + $CH_3COO^{\bullet}$) products increased the probability of $\mathbf{5}^{+\bullet}$ existing as a long-lived intermediate, whereas its interconversion with $\mathbf{7}^{+\bullet}$ via **TS5** was expected to favor the former on the basis of their relative Gibbs energies, $\Delta G_{310}(\mathbf{5}^{+\bullet} \rightarrow \mathbf{7}^{+\bullet})$ = 22 kJ mol^{-1} (Table 1). This is further discussed later in the paper by using the calculated rate constants.

The radical at 1′-C in in $\mathbf{7}^{+\bullet}$ may suggest weakening of the 3′-C−4′-C bond to possibly facilitate a competitive loss of an isomeric $C_2H_3O_2$ radical in the form of $HOCH_2CO^{\bullet}$. However, this was excluded by deuterium labeling experiments that showed no deuterium incorporation in the $C_2H_3O_2$ radical eliminated from $\mathbf{A}_{\mathbf{D5}}^{+\bullet}$ (Figure 4).

An alternative pathway for the ring opening in $\mathbf{5}^{+\bullet}$ was considered to proceed by radical-facilitated cleavage of the adjacent 3′-C−4′-C bond via **TS7** (Scheme 8). The calculated **TS7** energy (170 kJ mol^{-1} relative to $\mathbf{5}^{+\bullet}$) was substantially higher than that of **TS5**, and also the open-ring intermediate $\mathbf{10}^{+\bullet}$ was destabilized against $\mathbf{5}^{+\bullet}$. The energy data indicated that this alternative pathway was unlikely to be competitive with the pathway initiated by cleavage of the 1′-C−O bond shown in Scheme 7.

Isomerization and Dissociation Kinetics. We used the calculated TS structures and energies to assess the kinetics of the competitive hydrogen atom transfers onto the 2′-O-acetyl radical in $\mathbf{1}^{+\bullet}$ and its isotopologues. The RRKM rate constants for the hydrogen atom migrations from 1′-C, 2′-C, 3′-C, and 4′-C, denoted as $k_{1'\text{-H}}$, $k_{2'\text{-H}}$, $k_{3'\text{-H}}$, and $k_{4'\text{-H}}$, respectively, are plotted in Figure 7a. Consistent with its lowest **TS4** energy, the migration of 4′-H was kinetically favored, giving the largest rate constant over the entire energy scale. The relative rate constant, $k_{rel}(4'\text{-H}) = k_{4'\text{-H}}/(k_{1'\text{-H}} + k_{2'\text{-H}} + k_{3'\text{-H}} + k_{4'\text{-H}})$, indicated that 4′-H migration should be a dominant process, contributing >80% over most of the energy scale (Figure 7b). Isotope effects were considered for the migration of 4′-D that were relevant for the experimental fraction of 4′-D transfer. The $k_{rel}(4'\text{-D})$ in Figure 7b showed that even in the presence

https://doi.org/10.1021/jasms.4c00198
J. Am. Soc. Mass Spectrom. 2024, 35, 1594−1608

Scheme 7. Ring Opening in 4′-Radical $5^{+\bullet}$ and Loss of Acetoxyl Radical

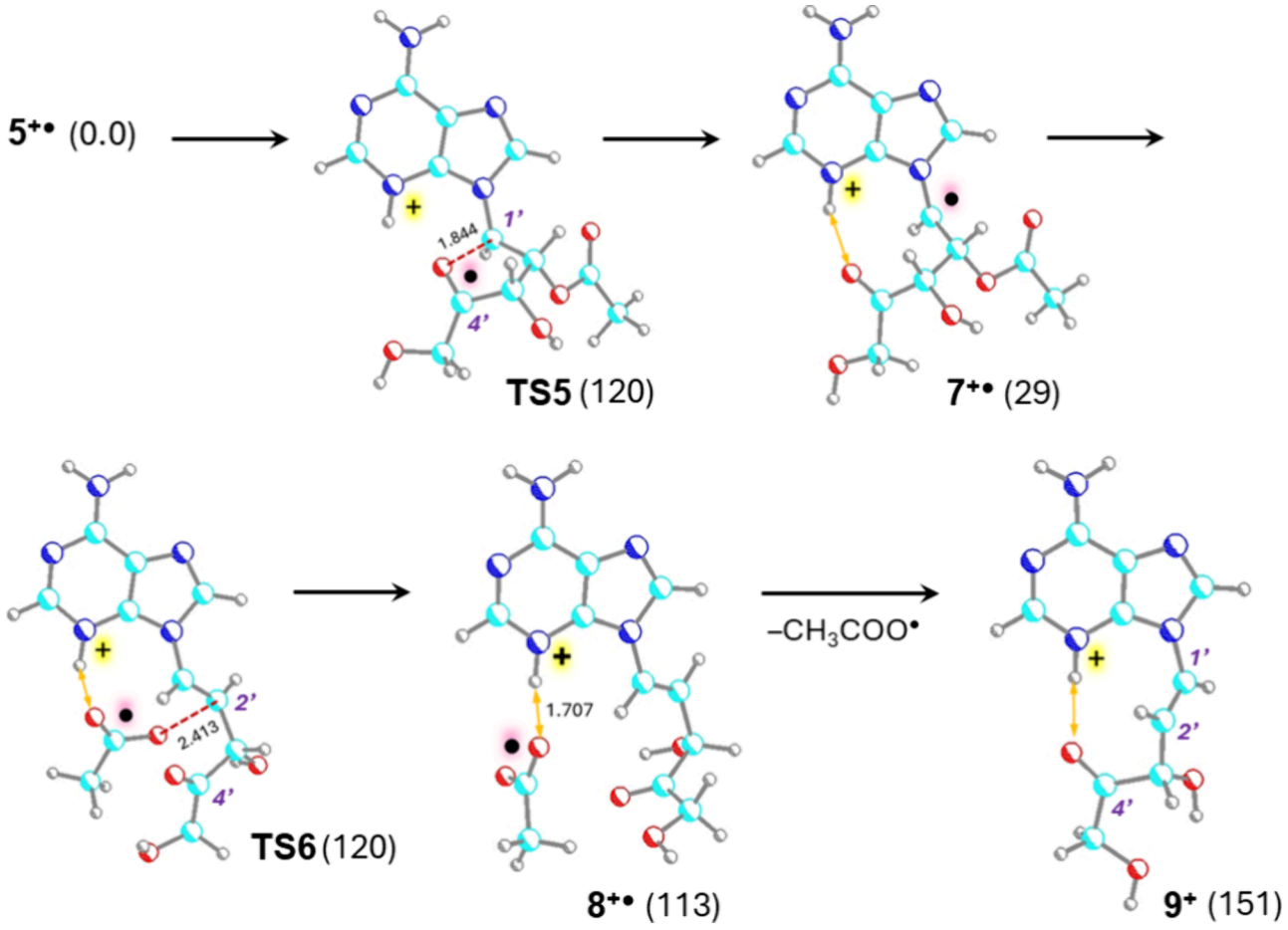

Scheme 8. Alternative Pathway for the Ring Opening in 4′-Radical $5^{+\bullet}$

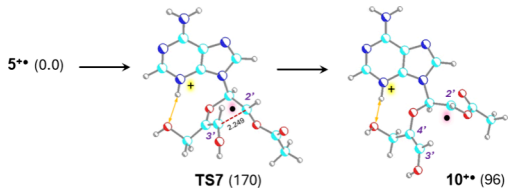

of a primary isotope effect, 4′-D should amount to >60% of all hydrogen transfer.

This RRKM-based result was somewhat higher than the 55% fraction of 4′-D migration that was indicated by the loss of $CH_2DCOO^{\bullet}$ from $\mathbf{A}_{4'\text{-D}}$ (Figure 4). A plot of the calculated primary and secondary isotope effects (Figure S4) showed that the primary isotope effect for the 4′-D migration, expressed as $k_{4'\text{-H}}/k_{4'\text{-D}}$, converged to ca. 2 at the highest energies, while the higher order isotope effect of 4′-D on the competitive 1′-H migration was very small (<1.04). This meant that the fraction of 4′-D migration was predicted not to significantly decrease even at high internal energies to make up the difference between the calculated fraction of k_{rel}(4′-D) and the fraction determined experimentally on the basis of the $CH_2DCOO^{\bullet}$ loss. The difference between the calculated and the experimental branching ratios for the 4′-D migration was likely due to minor inaccuracies in the calculated TS energies. Although M06-2X potential energy surfaces for nucleobase and nucleoside radicals have been previously found to be semiquantitatively accurate, as established by matching them against CCSD(T)/6-311++G(3df,2p) and CCSD(T)/complete basis set energies,[25,32] even minor energy adjustments in a few kJ mol^{-1} range would lead to significant changes in the calculated absolute and relative relative constants.

The 4′-H transfer showed a significant kinetic shift,[61] expressed as the difference between the internal energy needed to observe dissociation on the experimental time scale and the threshold energy defined by E(**TS4**). Considering a 0.05 s time scale for ion trap dissociations, >50% dissociation would require internal energies of ≥236 kJ mol^{-1} (Figure 7b), indicating a kinetic shift of $\Delta E_{kin} \geq 236-124 = 108$ kJ mol^{-1} for the fastest hydrogen transfer.

Ring opening in $\mathbf{5}^{+\bullet}$ required only 120 kJ mol^{-1} in **TS5**, which was below the dissociation threshold for the loss of acetoxyl radical (Scheme 7). This raised the possibility of reversible isomerization of $\mathbf{5}^{+\bullet}$ and the open-ring intermediate $\mathbf{7}^{+\bullet}$ prior to further 2′-C–2′-O bond dissociation via **TS6**, affecting the overall dissociation kinetics. The RRKM rate constants for the $\mathbf{5}^{+\bullet} \rightarrow \mathbf{7}^{+\bullet}$ and reverse $\mathbf{7}^{+\bullet} \rightarrow \mathbf{5}^{+\bullet}$ isomerization's, k_5 and k_{-5}, respectively, favored the reverse ring closure up to 350 kJ mol^{-1} internal energy, keeping a larger fraction of the intermediates as the ring-closed ion $\mathbf{5}^{+\bullet}$ (Figure 8a). Since both $\mathbf{5}^{+\bullet}$ and $\mathbf{7}^{+\bullet}$ are intermediates produced from $\mathbf{1}^{+\bullet}$ via **TS4**, the rate of their formation from the precursor needs to be considered. From the Figure 7b data it followed that achieving a ≥1% conversion of $\mathbf{1}^{+\bullet}$ to $\mathbf{5}^{+\bullet}$ required an internal energy of $E \geq 190$ kJ mol^{-1} relative to $\mathbf{5}^{+\bullet}$. Considering a >100 kJ mol^{-1} kinetic shift for the final

https://doi.org/10.1021/jasms.4c00198
J. Am. Soc. Mass Spectrom. 2024, 35, 1594−1608

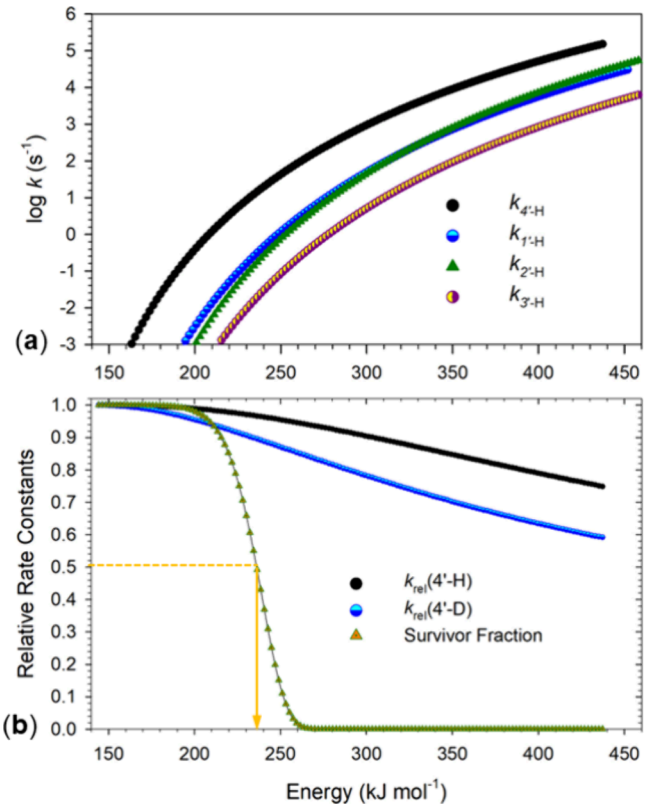

Figure 7. (a) RRKM rate constants for competitive hydrogen atom migrations in $\mathbf{1}^{+\bullet}$; (b) relative rate constants for 4′-H and 4′-D migrations and the energy-dependent fraction of $\mathbf{1}^{+\bullet}$ surviving after 50 ms.

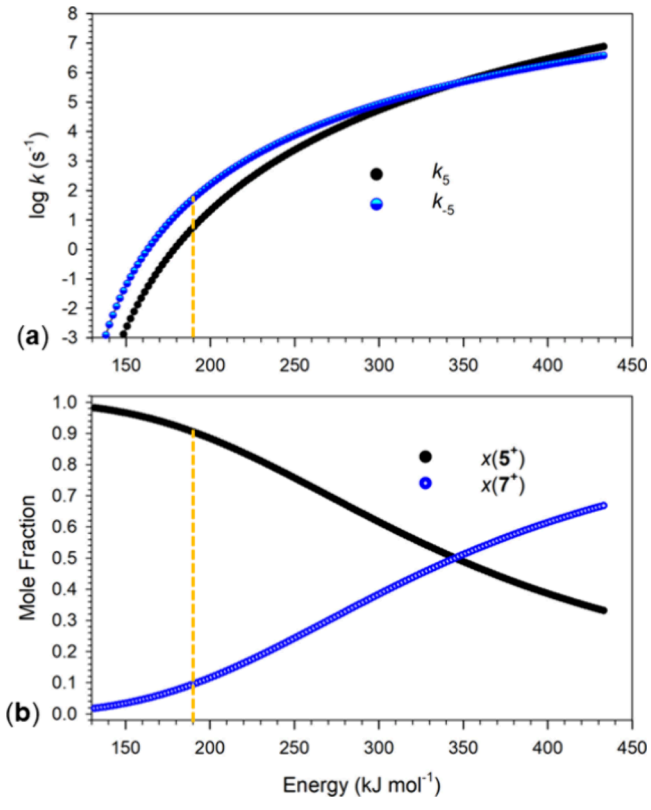

Figure 8. (a) RRKM rate constants for the reversible hydrogen atom migrations in $\mathbf{5}^{+\bullet}$ and $\mathbf{7}^{+\bullet}$; (b) mole fractions of $\mathbf{5}^{+\bullet}$ and $\mathbf{7}^{+\bullet}$ as a function of internal energy on a scale related to $\mathbf{5}^{+\bullet}$. The vertical dashed lines show the 1% kinetic threshold for the $\mathbf{5}^{+\bullet}$ formation from $\mathbf{1}^{+\bullet}$.

dissociation, leading to >250 kJ mol^{-1} internal energy in dissociating $\mathbf{5}^{+\bullet}$, the fast equilibration of $\mathbf{5}^{+\bullet}$ and $\mathbf{7}^{+\bullet}$ should still favor the former.

An interesting corollary of the Scheme 7 kinetics was that the acetoxyl radical in complex $\mathbf{8}^{+\bullet}$ did not efficiently abstract a hydrogen atom from ion $\mathbf{9}^{+}$ to form acetic acid, which would be an exothermic reaction. This was evidenced by the low relative intensity of the $(\mathbf{A} - CH_3COOH)^{+\bullet}$ fragment ion (4−5%) in all CID-MS^4 spectra in Figure 4. This indicated that the separation of $CH_3COO^{\bullet}$ and $\mathbf{9}^{+}$ in $\mathbf{7}^{+\bullet}$ was faster than the competitive hydrogen atom abstraction.

Relevant to the experimental conditions in the ion trap where ions undergo multiple collisions with the bath gas, we also considered the isomerization and dissociation kinetics under the high-pressure limit, as characterized by transition-state theory (TST).[53] The rate constants were calculated for the 1′-H, 1′-D, 4′-H, and 4′-D migrations, as plotted in Figure S5a (Supporting Information). Both reactions were affected by primary deuterium isotope effects, k_H/k_D, that ranged between 2.2 and 2.8 for both the 1′-H/D and the 4′-H/D migrations. The calculated isotope effects increased to 2.6−3.6 for both 1′-H/D and 4′-H/D migrations upon inclusion of quantum tunneling (Figure S5b).[56] This was consistent with the potential energy profiles for both migrations that were obtained from intrinsic reaction coordinate calculations[57] using M06-2X/6-31+G(d,p) in which both energy barriers showed very similar widths (Figure 9a). The TST branching ratio for the 1′-H migration was calculated as $k_{1'\text{-H}}(\text{rel}) = k_{1'\text{-H}}/(k_{1'\text{-H}} + k_{4'\text{-D}})$ for competition with the 4′-D migration, which was relevant for the ion relative intensities in the Figure 4 spectrum.

The calculated $k_{1'-\text{H}}(\text{rel})$ ranged between 0.1 and 0.2, accounting for the fraction of 1′-H migration in competition with the major 4′-D migration. This fraction was substantially lowered for the 1′-D migration competing with 4′-H, $k_{1'\text{-D}}(\text{rel}) = k_{1'\text{-D}}/(k_{1'\text{-D}} + k_{4'\text{-H}}) = 0.01-0.04$ (Figure 9b), which was compatible with the Figure 4 data for $\mathbf{A}_{1'\text{-D}}^{+\bullet}$. However, the TST analysis showed that isotope effects alone could not account for the low fraction of 4′-D migration, as shown by the CID spectra. The calculated mole fractions of $\mathbf{A}^{+\bullet}$ reacting on the 50 ms time scale (Figure 9b) indicated >50% conversion at effective temperatures T > 580 K, which appeared reasonable for ion excitation under ion trap conditions.[62−65]

UV−Vis Action Spectroscopy. The results from the isomerization kinetics raised the question of the nature of $\mathbf{A}^{+\bullet}$ generated and stored in the ion trap with respect to its retaining the acetoxyl radical structure $\mathbf{1}^{+\bullet}$ or undergoing spontaneous isomerization to ribose-ring radicals $\mathbf{2}^{+\bullet}-\mathbf{5}^{+\bullet}$. We addressed this question by measuring the UV−vis photodissociation (UVPD) action spectrum of $\mathbf{A}^{+\bullet}$ (m/z 309) that was generated in the ion source by the CID-MS^3 sequence (Scheme 2). The UVPD action spectrum was obtained in the 210−700 nm wavelength region covering valence electron excitations. No photon absorption leading to photodissociation was observed above 400 nm (<3.1 eV). The spectrum (Figure 10a) showed a strong composite band consisting of two components with maxima at 260 and 280 nm. The separate maxima were evident from the m/z 136 channel that also

https://doi.org/10.1021/jasms.4c00198
J. Am. Soc. Mass Spectrom. 2024, 35, 1594−1608

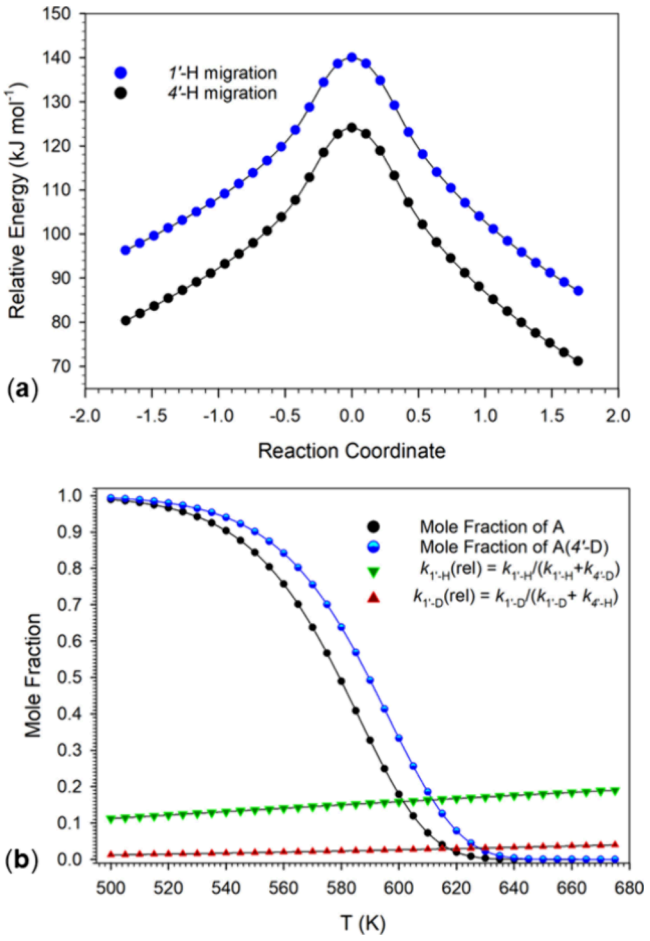

Figure 9. (a) Potential energy profiles for the 1′-H and 4′-H migrations in $\mathbf{1}^{+\bullet}$. The reaction coordinate is in mass-weighed internal coordinates relative to the pertinent transition state; (b) mole fractions of $\mathbf{1}^{+\bullet}$ and (4′-D)-$\mathbf{1}^{+\bullet}$ remaining after 50 ms. Branching ratios for the 1′-H and 1′-D transfer were calculated as the respective $k_{1'\text{-H}}$(rel) and $k_{1'\text{-D}}$(rel) relative TST rate constants.

showed a weak band at 212 nm. In addition, there was a broad band with a maximum at 330 nm that was observed chiefly in the *m*/*z* 164 ion channel. The calculated vibronic absorption spectra of $\mathbf{1}^{+\bullet}$, $\mathbf{2}^{+\bullet}$, $\mathbf{3}^{+\bullet}$, and $\mathbf{5}^{+\bullet}$ (Figure 10b–d) showed major bands with maxima at 240–260 nm that arose from vertical excitations in the 230–240 nm region. The vibronic envelopes of these major bands showed some distinctive features. For example, the spectrum of $\mathbf{1}^{+\bullet}$ (Figure 10b) showed two bands at 252 and 270 nm that were reminiscent of the split band in the action spectrum (Figure 10a). Perhaps more structurally significant was the broad band at 330 nm that had no analogy in the vibronic spectrum of $\mathbf{1}^{+\bullet}$. Absorption in the 300–360 nm region was calculated for the vibronic spectrum of $\mathbf{2}^{+\bullet}$. This was analogous to other adenine ions having a radical at 1′-C, such as in 9-methylene (1*H*) adenine cation radical,[66] in which the radical p orbital was conjugated with the adenine π-electronic system, leading to a lower excitation energy. The formation of $\mathbf{2}^{+\bullet}$ was qualitatively consistent with the calculated rate constants for the hydrogen transfer kinetics that predicted $\mathbf{2}^{+\bullet}$ as a minor product. In view of the isotope labeling results and theoretical rate constants for hydrogen migration, the action spectrum of $\mathbf{A}^{+\bullet}$ can be interpreted as representing a mixture of 2′-*O*-acetyl radical $\mathbf{1}^{+\bullet}$ and ribose radicals $\mathbf{2}^{+\bullet}$ and $\mathbf{5}^{+\bullet}$.

A salient feature of the adenosine cation radical dissociations was the directing effect of the ribose radical site created by hydrogen transfer to the acetoxyl radical. In 5′-*O*-acetyl radicals, a dominant transfer of 3′-H produced a 3′-C radical intermediate that underwent ring cleavage by consecutive 4′-C–O and 1′-C–2′-C bond dissociations, resulting in the formation of the 9-formyladenine cation as a major product.[32] Notably, 4′-H was nonreactive, and losses of acetyl and acetoxyl radicals were only minor dissociations of 5′-*O*-acetyladenosine radicals. In the 2′-*O*-acetyl radical $\mathbf{1}^{+\bullet}$, the hydrogen migration involved 4′-H, creating the 4′-C radical intermediate ($\mathbf{5}^{+\bullet}$) that initiated ring cleavage by 1′-C–O bond dissociation, resulting in the dominant loss of $CH_3COO^{\bullet}$ (Scheme 7). Thus, the position of the radical in the ring was the determining reactivity factor.

The $CH_3CO^{\bullet}$ radical formed in CID-MS^2 of $\mathbf{A}^{+\bullet}$ (Figure 2) rather unexpectedly did not include hydrogen atoms from 1′-, 2′-, 4′-C, or OH and NH, as established by deuterium labeling (Figure 5). This indicated that the formation of $CH_3CO^{\bullet}$ proceeded via a different mechanism than that of the related $CH_3COO^{\bullet}$, which involved 4′-H migration via **TS4** (Scheme 6). We tentatively propose that $CH_3CO^{\bullet}$ was formed in two steps as sketched in Scheme 9. The first step could involve homolytic cleavage of the 2′-O–$COCH_2^{\bullet}$ bond in $\mathbf{1}^{+\bullet}$ forming ketene in a complex with the adenosine radical. This would remove the steric constraints of the 2′-O–$COCH_2^{\bullet}$ ring configuration, allowing the ketene molecule to reach to more remote ribose positions for hydrogen atom transfer. Energetically, the 0 K ketene hydrogen atom affinity forming $CH_3CO^{\bullet}$ was calculated as 239 kJ mol^{-1} (based on CCSD(T)/complete basis set + zero-point vibrational energies), which was competitive for abstracting a hydrogen atom from the ribose radical. However, establishing a definite mechanism for the acetyl radical formation from $\mathbf{A}^{+\bullet}$ would require more extensive isotope labeling in all ribose positions along with product ion structure analysis.

Cation Radicals of Guanosine, Cytidine, and Thymidine. We employed the radical initiator method to generate other 2′-*O*-acetylnucleoside radicals. The nucleoside conjugates of guanosine, cytidine, and thymidine, $\mathbf{G}_p$, $\mathbf{C}_p$, and $\mathbf{T}_p$, respectively (Scheme 2), were synthesized analogously to the adenosine conjugate $\mathbf{A}_p$. Gas-phase cations were produced by electrospray ionization and subjected to CID for radical generation. The CID-MS^n spectra of the protonated guanosine conjugate and its dissociation intermediates are shown in Figure 11a–c. The CID-MS^2 spectrum of the conjugate ($\mathbf{G}_p$ + $H)^+$, *m*/*z* 573) resulted in a side-chain dissociation associated with the loss of N_2 that produced the intermediate ion at *m*/*z* 392 (Figure 11a). However, this desired dissociation competed with the glycosidic bond cleavage by loss of guanine (*m*/*z* 394), which was the major channel. CID-MS^3 of *m*/*z* 392 resulted in the loss of C_4H_5N, forming the 2′-*O*-acetylguanosine cation radical at *m*/*z* 325, as established by its accurate mass (Figure 11b). The spectrum showed that the side-chain cleavage in the *m*/*z* 392 intermediate was in part outcompeted by the glycosidic bond cleavage, forming protonated guanine at *m*/*z* 152 (Figure 11b). CID-MS^4 of mass-selected *m*/*z* 325 again resulted in a dominant glycosidic bond cleavage, forming competitively protonated guanine (*m*/*z* 152) and guanine cation radical (*m*/*z* 151). Dissociations that were triggered by the acetoxyl radical resulted in the competitive loss of $C_2H_3O^{\bullet}$ and $C_2H_3O_2^{\bullet}$ to give ions at *m*/*z* 282 and 266, respectively (Figure 11c). These were analogous to the *m*/*z* 266 and 250

https://doi.org/10.1021/jasms.4c00198
J. Am. Soc. Mass Spectrom. 2024, 35, 1594–1608

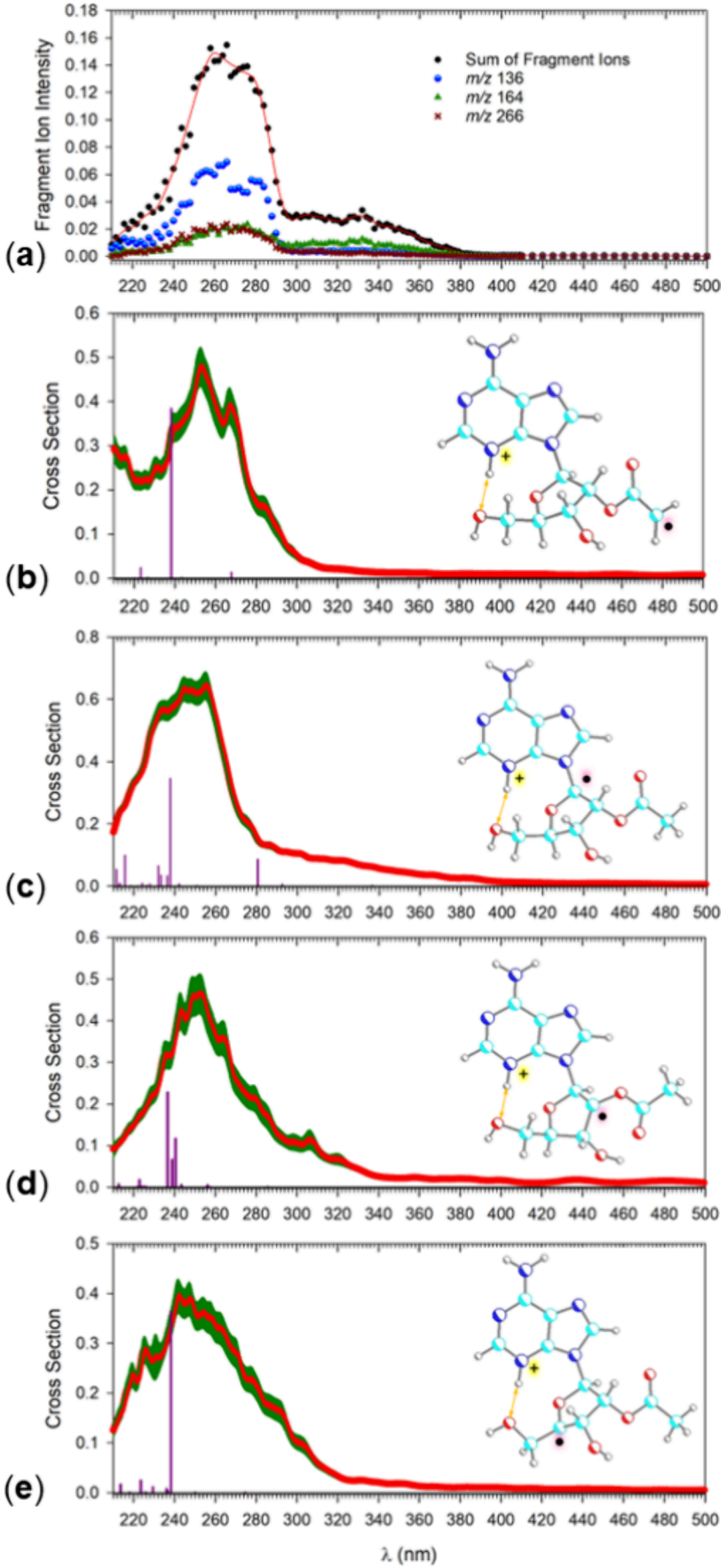

Figure 10. (a) UV−vis action spectrum of $\mathbf{A}^{+\bullet}$. Vibronic absorption spectra of (b) $\mathbf{1}^{+\bullet}$, (c) $\mathbf{2}^{+\bullet}$, (d) $\mathbf{3}^{+\bullet}$, and (e) $\mathbf{5}^{+\bullet}$. Vertical lines show 0 K electron transitions from M06-2X/6-31+G(d,p) TD-DFT calculations.

https://doi.org/10.1021/jasms.4c00198
J. Am. Soc. Mass Spectrom. 2024, 35, 1594−1608

Scheme 9. Proposed Mechanism for the Loss of $CH_3CO^{\bullet}$ from $1^{+\bullet}$

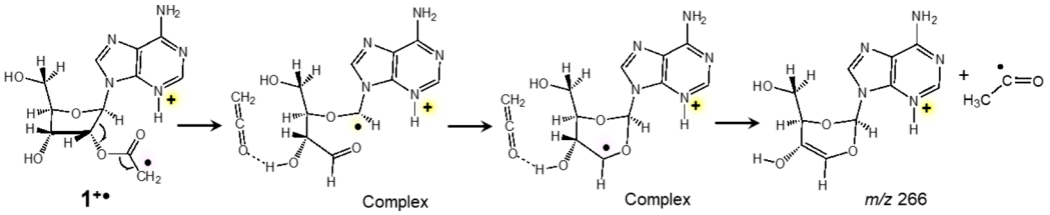

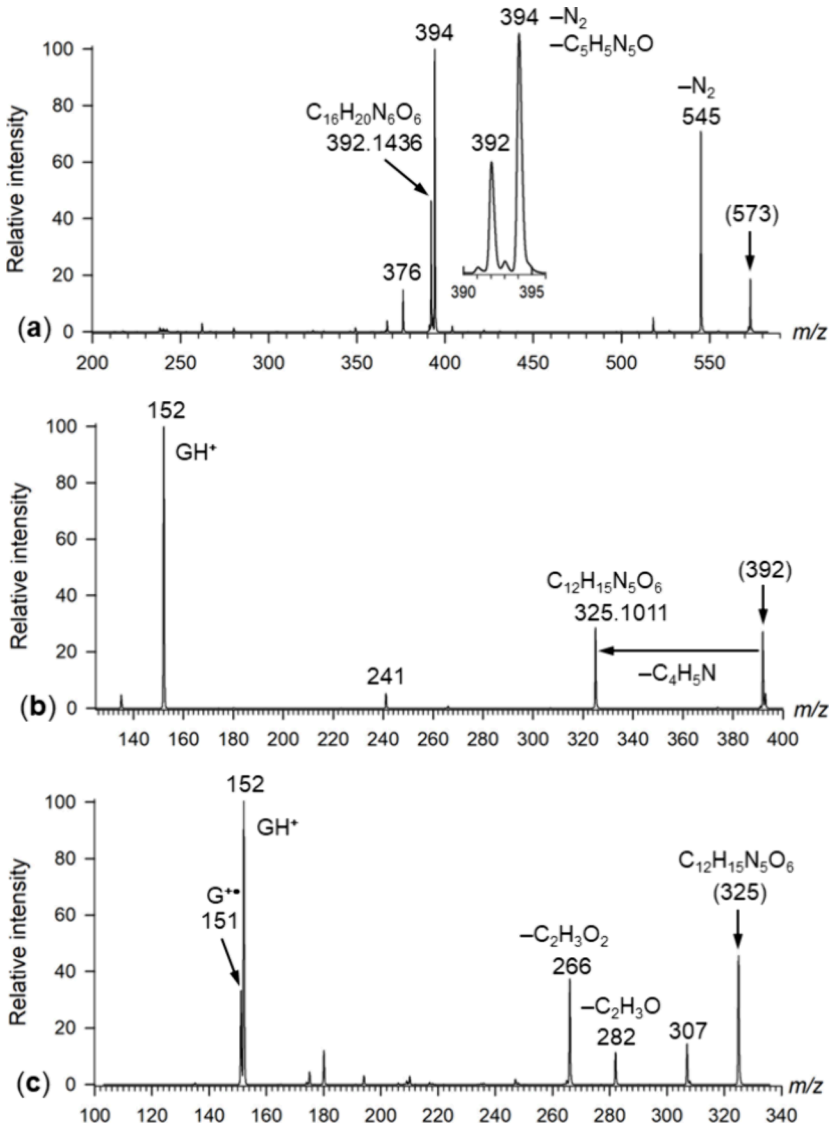

Figure 11. (a) CID-MS^2 of $(G_p + H)^+$ (m/z 573). (b) CID-MS^3 of the m/z 392 intermediate showing the formation of the 2′-*O*-acetylguanosine cation radical at m/z 325. (c) CID-MS^4 of m/z 325.

ions from CID of $A^{+\bullet}$ (Figure 2), indicating that the radical initiator technique could be employed to study hydrogen atom abstraction in guanosine cation radicals. However, the overall low efficiency of the radical reactions was an impediment to a detailed mechanistic study.

Investigations of the formation and properties of 2′-*O*-acetylcytidine and 2′-*O*-acetylthymidine cation radicals followed the above-outlined approach for adenosine and guanosine. CID-MS^n of the protonated cytidine conjugate $(C_p + H)^+$ (m/z 533) resulted in side-chain cleavage (m/z 352, Figure 12a) which, however, was a minor dissociation. The main products were formed by glycosidic bond cleavage and loss of cytosine (m/z 394, 376), as established by accurate mass measurements. CID-MS^3 of the m/z 352 intermediate also resulted in a dominant glycosidic bond cleavage, yielding the m/z 241.0933 (loss of cytosine) and 112.0500 ($C_4H_6N_3O$, protonated cytosine) ions along with the desired m/z 285.0942 ion ($C_{11}H_{15}N_3O_6$, Figure 12b). Finally, CID-MS^4 of the mass-selected m/z 285 ion chiefly showed glycosidic bond cleavage, forming the cytosine ion (m/z 112) and only minor products of radical-induced loss of $C_2H_3O^{\bullet}$ and $C_2H_3O_2^{\bullet}$ (Figure 12c).

https://doi.org/10.1021/jasms.4c00198
J. Am. Soc. Mass Spectrom. 2024, 35, 1594−1608

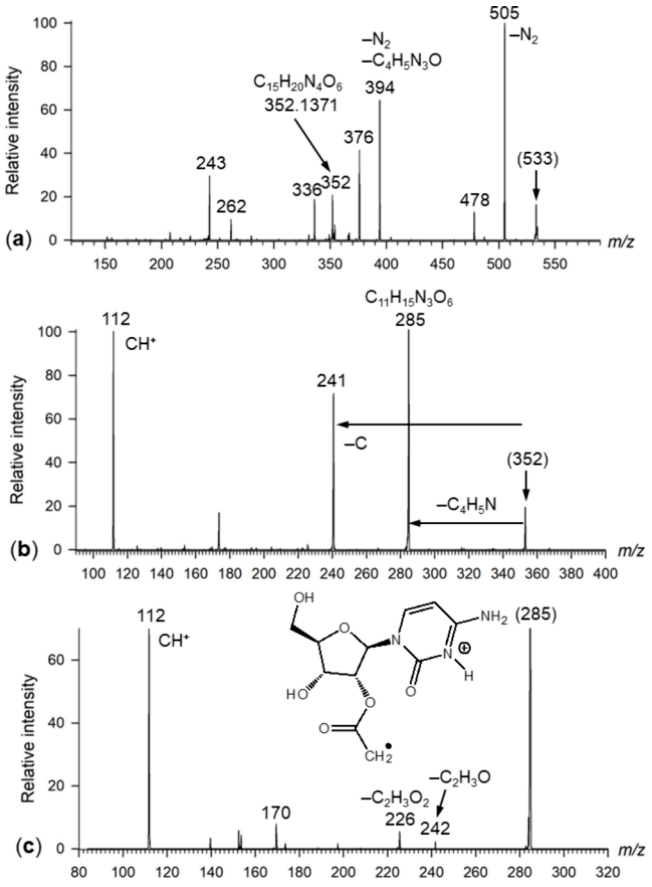

Figure 12. (a) CID-MS^2 of $(\mathbf{C}_p + H)^+$ (m/z 533). (b) CID-MS^3 of the m/z 352 intermediate showing the formation of the 2′-*O*-acetylcytidine cation radical at m/z 285. (c) CID-MS^4 of m/z 285.

CID-MS^n of the thymidine conjugate $(\mathbf{T}_p + H)^+$ at m/z 521 resulted in several competing dissociations by loss of water, thymine, and N_2 (Figure S6, Supporting Information). Although a $C_{16}H_{20}N_3O_6^{+\bullet}$ intermediate from side-chain dissociation was formed, it was not further investigated because of its low intensity and the overall complexity of the spectrum.

The different behavior upon CID of the adenosine, guanosine, and cytidine cation radicals can be related to the stability of the glycosidic bonds in the nucleoside ions that dissociate in competition with the azoalkane C−N═N−C bond cleavages triggering the dissociation of the side chain. The azoalkane dissociation in the ion conjugates can be considered a charge-remote reaction that is analogous to thermolysis of azoalkanes. The pertinent energy data have been known from the thermolysis of 4,4′-azobis(4-cyanopentanoic acid) in aqueous solution for which an activation energy was measured as E_a = 132.2 kJ mol^{-1}.[67] Another analogue, *tert*-butyldiazapropadiene, had E_a = 124.7 kJ mol^{-1}.[68] These energies can be compared to the threshold energies measured by Wu and Rodgers for CID of protonated adenosine (164 kJ mol^{-1}),[69] guanosine (115 kJ mol^{-1}),[70] and cytidine (112 kJ mol^{-1}),[71] forming the corresponding protonated nucleobases. According to the energy data, azoalkane side-chain dissociation was expected to predominate in the adenosine conjugate $(\mathbf{A}_p + H)^+$, as indeed observed in the Figure S1 spectrum (Supporting Information). The decreasing formation of intermediates of azoalkane side-chain cleavage from $(\mathbf{G}_p + H)^+$ and $(\mathbf{C}_p + H)^+$ (Figures 11a and 12a, respectively) was consistent with the low dissociation energies for the competing formation of protonated guanine and cytosine according to the Wu and Rodgers data.[70,71] Interestingly, glycosidic bond cleavage was also favored in guanine and cytosine radical intermediates, as shown in Figures 11b and 11c and 12b and 12c, respectively, but not in the adenine intermediates (Figure S1b, Supporting Information). Both the energy threshold for the loss of acetoxyl radical (125 kJ mol^{-1}, Table 1) and the lowest TS for the 4′-H migration in $\mathbf{1}^{+\bullet}$ (124 kJ mol^{-1}, Table 1) were below the energy needed for the adenine ion formation, presuming that the glycosidic bond cleavage in the adenosine ion was not significantly affected by the 2′-*O*-acetyl radical. The fact that the radical-driven reactions competed with the glycosidic bond cleavage in 2′-*O*-acetylguanosine and 2′-*O*-acetylcytidine cation radicals indicated that their energetics were similar to that in $\mathbf{1}^{+\bullet}$, which was consistent with the above-mentioned energy data for protonated guanosine and cytidine.[70,71]

CONCLUSIONS

Adenosine 2′-*O*-acetyl radicals were found to undergo specific transfer of 4′-H that triggered ring cleavage and loss of acetoxyl radical. In parallel, the cation radicals underwent loss of acetyl radical that, however, did not involve hydrogen transfer from 1′-H, 2′-H, and 4′-H and likely proceeded by a different mechanism involving ion−molecule complexes. By comparing radical dissociations in isomeric 2′-*O*-acetyl and 5′-*O*-acetyladenosine cation radicals, we can conclude that the radical reactions are regiospecific as well as stereospecific. The regiospecificity affected the final product formation that differed for the isomeric radicals. The stereospecificity affected the transition-state energies that determined the reaction kinetics. Energy and kinetic analysis of the dissociation reactions in both 2′-*O*-acetyl and 5′-*O*-acetyladenosine cation radicals indicated that intramolecular hydrogen transfer was the rate-determining step for both radical systems. The regiospecificity and energetics of these reactions represent benchmarks for intermolecular radical reactions relevant to nucleic acid damage.

ASSOCIATED CONTENT

Supporting Information

The Supporting Information is available free of charge at https://pubs.acs.org/doi/10.1021/jasms.4c00198.

Description of synthetic procedures with compound spectroscopic characterization, additional figures including NMR and mass spectra, reaction schemes, and energies from DFT calculations (PDF)

AUTHOR INFORMATION

Corresponding Author

František Tureček − *Department of Chemistry, University of Washington, Seattle, Washington 98195-1700, United States*; Phone: 206-685-2041; Email: turecek@uw.edu

Authors

Václav Zima − *Department of Chemistry, University of Washington, Seattle, Washington 98195-1700, United States; Institute of Organic Chemistry and Biochemistry, Czech Academy of Sciences, 166 10 Prague, Czech Republic*

Owen Gladwish − *Department of Chemistry, Case Western Reserve University, Cleveland, Ohio 44106-7078, United States*

Aleš Marek − *Institute of Organic Chemistry and Biochemistry, Czech Academy of Sciences, 166 10 Prague, Czech Republic;* orcid.org/0000-0001-9031-8263

Complete contact information is available at: https://pubs.acs.org/10.1021/jasms.4c00198

Notes

The authors declare no competing financial interest.

■ ACKNOWLEDGMENTS

Support by the Chemistry Division of the U.S. National Science Foundation (Grant CHE-1951518) and the Klaus and Mary Ann Saegebarth Endowment is gratefully acknowledged. Research at the IOCB was supported by the Ministry of Education, Youth and Sport (MSMT INTER-EXCELLENCE LTAUSA19094).

■ REFERENCES

(1) von Sonntag, C.; Hagen, U.; Schon-Bopp, A.; Schulte-Frohlinde, D. Radiation-Induced Strand Breaks in DNA: Chemical and Enzymatic Analysis of End Groups and Mechanistic Aspects. *Adv. Radiat Biol.* **1981**, *9*, 109−142.

(2) von Sonntag, C. *Free-Radical-Induced DNA Damage and Its Repair*; Springer, 2006.

(3) Giese, B. Long-Distance Electron Transfer Through DNA. *Annu. Rev. Biochem.* **2002**, *71*, 51−70.

(4) Douki, T.; Ravanat, J.-L.; Angelov, D.; Wagner, J. R.; Cadet, J. Effects of Duplex Stability on Charge-Transfer Efficiency within DNA. In *Long-Range Charge Transfer in DNA I*; Schuster, G. B., Ed.; Springer Berlin Heidelberg: Berlin, Heidelberg, 2004; pp 1−25.

(5) Wagenknecht, H.-A.; Fiebig, T. *Charge Transfer in DNA*; John Wiley & Sons, Ltd., 2005.

(6) Kawai, K.; Majima, T. Hole Transfer Kinetics of DNA. *Acc. Chem. Res.* **2013**, *46* (11), 2616−2625.

(7) Khanna, K. K.; Jackson, S. P. DNA Double-Strand Breaks: Signaling, Repair and the Cancer Connection. *Nat. Genet.* **2001**, *27*, 247−254.

(8) Pogozelski, W. K.; Tullius, T. D. Oxidative Strand Scission of Nucleic Acids: Routes Initiated by Hydrogen Abstraction from the Sugar Moiety. *Chem. Rev.* **1998**, *98*, 1089−1108.

(9) Schuster, G. B. Long-Range Charge Transfer in DNA: Transient Structural Distortions Control the Distance Dependence. *Acc. Chem. Res.* **2000**, *33*, 253−260.

(10) Ito, T.; Kuno, S.; Uchida, T.; Fujita, S.; Nishimoto, S. Properties and Reactivity of the Adenosine Radical Generated by Radiation-Induced Oxidation in Aqueous Solution. *J. Phys. Chem. B* **2009**, *113*, 389−394.

(11) Peoples, A. R.; Mercer, K. R.; Bernhard, W. A. What Fraction of DNA Double-Strand Breaks Produced by the Direct Effect is Accounted for by Radical Pairs? *J. Phys. Chem. B* **2010**, *114*, 9283−9288.

(12) Taverna Porro, M. L.; Greenberg, M. M. DNA double strand cleavage via interstrand hydrogen atom abstraction. *J. Am. Chem. Soc.* **2013**, *135*, 16368−16371.

(13) Jovanovic, S. V.; Simic, M. G. One-Electron Redox Potentials of Purines and Pyrimidines. *J. Phys. Chem.* **1986**, *90*, 974−978.

(14) Steenken, S.; Jovanovic, S. V. How Easily Oxidizable Is DNA? One-Electron Reduction Potentials of Adenosine and Guanosine Radicals in Aqueous Solution. *J. Am. Chem. Soc.* **1997**, *119*, 617−618.

(15) Steenken, S. Purine Bases, Nucleosides, and Nucleotides: Aqueous Solution Redox Chemistry and Transformation Reactions of Their Radical Cations and e- and OH Adducts. *Chem. Rev.* **1989**, *89*, 503−520.

(16) Jimenez, Li. B.; Encinas, S.; Miranda, M. A.; Navacchia, M. L.; Chatgilialoglu, C. The Photochemistry of 8-Bromo-2'-deoxyadenosine. A Direct Entry to Cyclopurine Lesions. *Photochem. Photobiol. Sci.* **2004**, *3*, 1042−1046.

(17) Barnes, J.; Bernhard, W. A. The Protonation State of One-Electron Reduced Cytosine and Adenine. 1. Initial Protonation Sites at Low Temperatures in Glassy Solids. *J. Phys. Chem. A* **1993**, *97*, 3401−3408.

(18) Barnes, J.; Bernhard, W. A. One-Electron-Reduced Cytosine in Acidic Glasses: Conformational States before and after Proton Transfer. *J. Phys. Chem. A* **1994**, *98*, 10969−10977.

(19) Adhikary, A.; Khanduri, D.; Kumar, A.; Sevilla, M. D. Photoexcitation of Adenine Cation Radical [A·+] in the near UV-vis Region Produces Sugar Radicals in Adenosine and in Its Nucleotides. *J. Phys. Chem. B* **2008**, *112*, 15844−15855.

(20) Shukla, L. I.; Pazdro, R.; Huang, J.; DeVreugd, C.; Becker, D.; Sevilla, M. D. The Formation of DNA Sugar Radicals from Photoexcitation of Guanine Cation Radicals. *Radiat. Res.* **2004**, *161*, 582−590.

(21) Khanduri, D.; Collins, S.; Kumar, A.; Adhikary, A.; Sevilla, M. D. Formation of Sugar Radicals in RNA Model Systems and Oligomers via Excitation of Guanine Cation Radical. *J. Phys. Chem. B* **2008**, *112*, 2168−2178.

(22) Tureček, F. Flying DNA Cation Radicals in the Gas Phase: Generation and Action Spectroscopy of Canonical and Noncanonical Nucleobase Forms. *J. Phys. Chem. B* **2021**, *125*, 7090−7100.

(23) Antoine, R.; Dugourd, P. UV-visible Activation of Biomolecular Ions. In *Laser Photodissociation and Spectroscopy of Mass-Separated Biomolecular Ions, Lecture Notes in Chemistry*; Polfer, N. C., Dugourd, P., Eds.; Springer: Heidelberg, 2013; Vol. *83*, pp 93−116.

(24) Giles, K.; Ujma, J.; Wildgoose, J.; Pringle, S.; Richardson, K.; Langridge, D.; Green, M. A Cyclic Ion Mobility-Mass Spectrometry System. *Anal. Chem.* **2019**, *91*, 8564−8573.

(25) Zima, V.; Vlk, M.; Wan, J.; Cvačka, J.; Tureček, F. Tracking Isomerizations of High-Energy Adenine Cation Radicals by UV-Vis Action Spectroscopy and Cyclic Ion Mobility Mass Spectrometry. *J. Phys. Chem. A* **2023**, *127*, 5899−5913.

(26) Lesslie, M.; Lawler, J. T.; Dang, A.; Korn, J. A.; Bím, D.; Steinmetz, V.; Maitre, P.; Tureček, F.; Ryzhov, V. Cytosine radical cation: a gas-phase study combining IRMPD spectroscopy, UV-PD spectroscopy, ion−molecule reactions, and theoretical calculations. *ChemPhysChem* **2017**, *18*, 1293−1301.

(27) Korn, J. A.; Urban, J.; Dang, A.; Nguyen, H. T. H.; Tureček, F. UV-Vis Action Spectroscopy Reveals a Conformational Collapse in Hydrogen-Rich Dinucleotide Cation Radicals. *J. Phys. Chem. Lett.* **2017**, *8*, 4100−4107.

(28) Dang, A.; Nguyen, H. T. H.; Ruiz, H.; Piacentino, E.; Ryzhov, V.; Tureček, F. Experimental Evidence for Non-Canonical Thymine Cation Radicals in the Gas Phase. *J. Phys. Chem. B* **2018**, *122*, 86−97.

(29) Liu, Y.; Dang, A.; Urban, J.; Tureček, F. Charge-Tagged DNA Radicals in the Gas Phase Characterized by UV-Vis Photodissociation Action Spectroscopy. *Angew. Chem., Int. Ed. Engl.* **2020**, *59*, 7772−7777.

(30) Liu, Y.; Ma, C.; Leonen, C. J. A.; Chatterjee, C.; Nováková, G.; Marek, A.; Tureček, F. Tackling a Curious Case. Generation of Charge-Tagged Guanosine Radicals by Electron Transfer in the Gas Phase and Their Characterization by UV-Vis Photodissociation Action Spectroscopy and Theory. *J. Am. Soc. Mass Spectrom.* **2021**, *32*, 772−785.

(31) Liu, Y.; Ma, C.; Nováková, G.; Marek, A.; Tureček, F. Charge-Tagged Nucleosides in the Gas Phase: UV-Vis Action Spectroscopy and Structures of Cytidine Cations, Dications, and Cation Radicals. *J. Phys. Chem. A* **2021**, *125*, 6096−6108.

(32) Zima, V.; Marek, A.; Tureček, F. Competitive Radical Migrations and Ribose Ring Cleavage in Adenosine and 2'-Deoxyadenosine Cation Radicals. *J. Phys. Chem. A* **2024**, *128*, 1109−1123.

(33) Wu, R. R.; Rodgers, M. T. Mechanisms and Energetics for N-Glycosidic Bond Cleavage of Protonated Adenine Nucleosides: N3

Protonation Induces Base Rotation and Enhances N-Glycosidic Bond Stability. *Phys. Chem. Chem. Phys.* **2016**, *18*, 16021−16032.
(34) Hodyss, R.; Cox, H. A.; Beauchamp, J. L. Bioconjugates for Tunable Peptide Fragmentation: Free Radical Initiated Peptide Sequencing (FRIPS). *J. Am. Chem. Soc.* **2005**, *127*, 12436−12437.
(35) Desai, N.; Thomas, D. A.; Lee, J.; Gao, J.; Beauchamp, J. L. Eradicating Mass Spectrometric Glycan Rearrangement by Utilizing Free Radicals. *Chem. Sci.* **2016**, *7*, 5390−5397.
(36) Dang, A.; Korn, J. A.; Gladden, J.; Mozzone, B.; Tureček, F. "UV-Vis Photodissociation Action Spectroscopy on Thermo LTQ-XL ETD and Bruker amaZon Ion Trap Mass Spectrometers: A Practical Guide. *J. Am. Soc. Mass Spectrom.* **2019**, *30*, 1558−1564.
(37) Berendsen, H. J.; Postma, J. V.; van Gunsteren, W. F.; DiNola, A. R. H. J.; Haak, J. R. Molecular Dynamics with Coupling to an External Bath. *J. Chem. Phys.* **1984**, *81*, 3684−3690.
(38) Řezáč, J.; Fanfrlik, J.; Salahub, D.; Hobza, P. Semi-Empirical Quantum Chemical PM6Method Augmented by Dispersion and H Bonding Correction Terms Reliably Describes Various Types of Noncovalent Complexes. *J. Chem. Theory Comput.* **2009**, *5*, 1749−1760.
(39) Řezáč, J. Cuby: An Integrative Framework for Computational Chemistry. *J. Comput. Chem.* **2016**, *37*, 1230−1237.
(40) Stewart, J. J. P. *MOPAC 16*; Stewart Computational Chemistry: Colorado Springs, CO, 2016.
(41) Becke, A. D. Density-Functional Exchange-Energy Approximation with Correct Asymptotic Behavior. *Phys. Rev. A* **1988**, *38*, 3098−3100.
(42) Zhao, Y.; Truhlar, D. G. The M06 Suite of Density Functionals for Main Group Thermochemistry, Thermochemical Kinetics, Noncovalent Interactions, Excited States, and Transition Elements: Two New Functionals and Systematic Testing of Four M06-Class Functionals and 12 Other Functionals. *Theor. Chem. Acc.* **2008**, *120*, 215−241.
(43) Dunning, T. H., Jr Gaussian Basis Sets for Use in Correlated Molecular Calculations. I. The Atoms Boron Through Neon and Hydrogen. *J. Chem. Phys.* **1989**, *90*, 1007−1023.
(44) Weigend, F.; Ahlrichs, R. Balanced Basis Sets of Split Valence, Triple Zeta Valence and Quadruple Zeta Valence Quality for H to Rn. Design and Assessment of Accuracy. *Phys. Chem. Chem. Phys.* **2005**, *7*, 3297−3305.
(45) Weigend, F. Accurate Coulomb-Fitting Basis Sets for H to Rn. *Phys. Chem. Chem. Phys.* **2006**, *8*, 1057−1065.
(46) Furche, F.; Ahlrichs, A. Adiabatic Time-Dependent Density Functional Methods for Excited State Properties. *J. Chem. Phys.* **2002**, *117*, 7433−7447.
(47) Turecek, F. Benchmarking Electronic Excitation Energies and Transitions in Peptide Radicals. *J. Phys. Chem. A* **2015**, *119*, 10101−10111.
(48) Huang, S. R.; Dang, A.; Tureček, F. Ground and Excited States of Gas-Phase DNA Nucleobase Cation-Radicals. A UV-Vis Photodissociation Action Spectroscopy and Computational Study of Adenine and 9-Methyladenine. *J. Am. Soc. Mass Spectrom.* **2020**, *31*, 1271−1281.
(49) Reed, A. E.; Weinstock, R. B.; Weinhold, F. Natural Population Analysis. *J. Chem. Phys.* **1985**, *83*, 735−746.
(50) Wigner, E. On The Quantum Correction for Thermodynamic Equilibrium. *Phys. Rev.* **1932**, *40*, 749−759.
(51) Bonačić-Koutecký, V.; Mitrić, R. Theoretical Exploration of Ultrafast Dynamics in Atomic Clusters: Analysis and Control. *Chem. Rev.* **2005**, *105*, 11−66.
(52) Barbatti, M.; Ruckenbauer, M.; Plasser, F.; Pittner, J.; Granucci, G.; Persico, M.; Lischka, H. Newton-X: A Surface-Hopping Program for Nonadiabatic Molecular Dynamics. *Wiley Interdisciplinary Reviews: Comput. Mol. Sci.* **2014**, *4*, 26−33.
(53) Gilbert, R. G.; Smith, S. C. *Theory of Unimolecular and Recombination Reactions*; Blackwell Scientific Publications: Oxford, 1990; pp 52−132.
(54) Zhu, L.; Hase, W. L. *Quantum Chemistry Program Exchange, Program No. QCPE 644*; Indiana University: Bloomington, IN, 1994.
(55) Frank, A. J.; Sadilek, M.; Ferrier, J. G.; Turecek, F. Sulfur Oxoacids and Radicals in the Gas Phase. A Variable-Time Neutralization-Photoexcitation- Reionization Mass Spectrometric and Ab initio/RRKM Study. *J. Am. Chem. Soc.* **1997**, *119*, 12343−12353.
(56) Bell, R. P. *The Tunnel Effect in Chemistry*; Chapman and Hill: London, 1980; pp 21−26, 60−62.
(57) Gonzalez, C.; Schlegel, H. B. An Improved Algorithm for Reaction Path Following. *J. Chem. Phys.* **1989**, *90*, 2154−2161.
(58) Huang, S. R.; Tureček, F. Non-Canonical DNA Nucleoside Cation Radicals. A Computational Study of the Dark Matter of DNA Ionization. *J. Phys. Chem. B* **2022**, *126*, 2480−2497.
(59) Yates, B. F.; Bouma, W. J.; Radom, L. Distonic Radical Cations Guidelines for the Assessment of Their Stability. *Tetrahedron* **1986**, *42*, 6225−6234.
(60) Hammerum, S. Distonic Radical Cations in Gaseous and Condensed Phase. *Mass Spectrom. Rev.* **1988**, *7*, 123−202.
(61) Lifshitz, C. Time-Resolved Appearance Energies, Breakdown Graphs, and Mass Spectra: The Elusive Kinetic Shift. *Mass Spectrom. Rev.* **1982**, *1*, 309−348.
(62) Goeringer, D. E.; McLuckey, S. A. Evolution of Ion Internal Energy during Collisional Excitation in the Paul Ion Trap: A Stochastic Approach. *J. Chem. Phys.* **1996**, *104*, 2214−2221.
(63) Gronert, S. Estimation of Effective Ion Temperatures in a Quadrupole Ion Trap. *J. Am. Soc. Mass Spectrom.* **1998**, *9*, 845−848.
(64) Lovejoy, E. R.; Wilson, R. R. Kinetic Studies of Negative Ion Reactions in a Quadrupole Ion Trap: Absolute Rate Coefficients and Ion Energies. *J. Phys. Chem. A* **1998**, *102*, 2309−2315.
(65) Donald, W. A.; Khairallah, G. N.; O'Hair, R. A. J. The Effective Temperature of Ions Stored in a Linear Quadrupole Ion Trap Mass Spectrometer. *J. Am. Soc. Mass Spectrom.* **2013**, *24*, 811−815.
(66) Huang, S. R.; Nováková, G.; Marek, A.; Tureček, F. The Elusive Non-Canonical Isomers of Ionized 9-Methyladenine and 2'-Deoxyadenosine. *J. Phys. Chem. A* **2021**, *125*, 338−348.
(67) Zhou, Y.; Zhang, Z.; Postma, A.; Moad, G. Kinetics and Mechanism for Thermal and Photochemical Decomposition of 4,4'-Azobis(4-cyanopentanloic acid) in Aqueous Media. *Polym. Chem.* **2019**, *10*, 3284−3287.
(68) Crawford, R. J.; Takagi, K. Mechanism of Azoalkane Thermolysis. Concerted or Nonconcerted? *J. Am. Chem. Soc.* **1972**, *94*, 7406−7416.
(69) Wu, R. R.; Rodgers, M. T. Mechanisms and Energetics for N-Glycosidic Bond Cleavage of Protonated Adenine Nucleosides: N3 Protonation Induces Base Rotation and Enhances N-glycosidic Bond Stability. *Phys. Chem. Chem. Phys.* **2016**, *18*, 16021−16032.
(70) Wu, R. R.; Chen, Yu; Rodgers, M. T. Mechanisms and Energetics for N-Glycosidic Bond Cleavage of Protonated 2′-Deoxyguanosine and Guanosine. *Phys. Chem. Chem. Phys.* **2016**, *18*, 2968−2980.
(71) Wu, R. R.; Rodgers, M. T. O2 Protonation Controls Threshold Behavior for N-Glycosidic Bond Cleavage of Protonated Cytosine Nucleosides. *J. Phys. Chem. B* **2016**, *120*, 4803−4811.

https://doi.org/10.1021/jasms.4c00198
J. Am. Soc. Mass Spectrom. 2024, 35, 1594−1608